Generation and characterization of spectrally factorable biphotons

by

Changchen Chen

B.S. in Optical Engineering
B.A. in Physics
University of Rochester, 2015

Submitted to the Department of Electrical Engineering and Computer Science
in partial fulfillment of the requirements for the degree of

Master of Science in Electrical Engineering and Computer Science

at the

MASSACHUSETTS INSTITUTE OF TECHNOLOGY

June 2017

Author .....
Department of Electrical Engineering and Computer Science
May 19, 2017

Certified by .....
Franco N.C. Wong
Senior Research Scientist, Research Laboratory of Electronics
Thesis Supervisor

Accepted by .....
Leslie A. Kolodziejski
Professor of Electrical Engineering and Computer Science
Chair, Department Committee on Graduate Students

Generation and characterization of spectrally factorable biphotons

by

Changchen Chen

Submitted to the Department of Electrical Engineering and Computer Science
on May 19, 2017, in partial fulfillment of the
requirements for the degree of
Master of Science in Electrical Engineering and Computer Science

Abstract

Spectrally unentangled biphotons with high single-spatiotemporal-mode purity are highly desirable for many quantum information processing tasks. We generate biphotons with an inferred heralded-state spectral purity of 99%, the highest to date without any spectral filtering, by pulsed spontaneous parametric down-conversion (SPDC) in a custom-fabricated periodically-poled $KTiOPO_4$ (PPKTP) crystal under extended Gaussian phase-matching conditions. The high purity achieved is made possible by the Gaussian phase-matching function of our custom PPKTP crystal. Without applying spectral filtering and using a standard PPKTP crystal, the highest previously reported purity is 93%. We characterize the joint spectral density of the generated biphoton by converting the spectral content to temporal information via dispersion through a 42-km SMF28 fiber. To characterize the JSD at high spectral resolution and more efficiently, we employ a commercially available dispersion compensation module (DCM) with a dispersion equivalent to 100 km of standard optical fiber and with an insertion loss of only 2.8 dB. Compared with the typical method of using two temperature-stabilized equal-length fibers that incurs an insertion loss of 20 dB per fiber, the DCM approach achieves high spectral resolution in a much shorter measurement time. We also verify the indistinguishability of the SPDC signal and idler photons via Hong-Ou-Mandel interferometric measurements. The near perfect interference visibility confirms that they are indeed indistinguishable.

Thesis Supervisor: Franco N.C. Wong
Title: Senior Research Scientist, Research Laboratory of Electronics

Acknowledgments

I would like to first express my gratitude to Dr. Franco Wong. It is my privilege to have him as my advisor. Franco is extremely knowledgeable and always approachable. More importantly, he has been very supportive and encouraging from the very beginning of this project. His dedication, enthusiasm, and critical thinking make him a terrific role model to follow. I cannot imagine a better advisor than him.

I would also like to express my sincere gratitude to Prof. Jeff Shapiro for valuable discussions and guidance during the past two years. I am fortunate in having the opportunity to work with him.

I would like to say thank you to Prof. James Fujimoto for being a great academic advisor.

A special thank you to Bo Cao for his important contribution to this project. He has never hesitated to share his knowledge and experience with me. It is a really enjoyable experience working with him. I also would like to say thank you to Dr. Feihu Xu and Dr. Zheshen Zhang, from whom I have learned a great deal about how to be a good researcher. Their constructive suggestions and insightful comments have made this project much easier to do. This project and I are also greatly indebted to Murphy Niu's well-designed crystal and many of her valuable works. Last but not least, I would like to thank Dr. Ben Dixon for many helpful discussions on this project.

Thank you to Jane Heyes for many conversations we had about graduate school. I would also like to acknowledge all my friends at MIT for making graduate school hardship bearable.

I would like to express my appreciation to Tracy Tian, who has always encouraged me to achieve the most. Finally, I want to thank my parents for always believing in me and supporting me unconditionally in the past years.

This thesis is dedicated to my family.

Contents

List of Figures

List of Tables

Chapter 1

Introduction

1.1 Background and Motivation

Quantum computation can, in theory, solve certain problems much faster than classical computation. Such problems include prime number factoring [1], quantum system simulations [2, 3], and database searching [4]. In principle, quantum computation utilizes quantum mechanical features, such as entanglement and superposition, to perform computation in a massively parallel fashion and boost performance exponentially. Although quantum computation is still in its infancy today, its unfathomable potential in computational power offers a promising outlook.

A non-universal approach to demonstrate the computational advantage of quantum computation is boson sampling [5, 6, 7, 8]. Boson sampling targets a specific sampling problem of calculating the output probability of N identical photons when they are sent into a M-input, M-output linear optical circuit. Even though this seems to be a suitable mathematical problem for today's powerful computer, the actual solution involves calculating the permanent of a complex matrix, which is extremely hard to compute with a classical computer. The quantum solution for this problem is relatively straightforward. By physically performing the task, sending N identical photons through a series of beam splitters, the probability distribution at the output can be obtained by monitoring the exit ports of the system with photodetectors. The physical simulation automatically takes into account the computationally complex interference mechanism that occurs at every beam splitter.

To perform this experiment, a source that generates identical single photons is required. However, getting all photons to be identical in every aspect is difficult. Some photon features are easy to control and maintain, such as selecting polarizations with wave plates and polarizers, and spatial modes with single-mode fibers or waveguides. Other aspects, such as photon spectra and times of arrival at the interference locations, are not as simple to manipulate. In this thesis, a biphoton source that can yield indistinguishable heralded single photons is considered. This potential source of single-spatiotemporal-mode photons can be adopted in many other photonic quantum information processing (QIP) applications besides boson sampling, such as quantum computation [9, 10] and quantum repeaters for long-distance quantum communication networks [11, 12], whose measurement-based protocols rely on high-interference visibility between individual indistinguishable photons.

Consider the widely used method of generating heralded single photons by pulsed spontaneous parametric down-conversion (SPDC) in a nonlinear optical crystal. Typical SPDC outputs consist of pairs of spectrally entangled signal and idler photons whose biphoton state has a Schmidt number greater than 1 under Schmidt decomposition [13, 14]. The detection of the idler photon of the spectrally entangled biphoton heralds the presence of the signal photon; however, the heralded signal photon is in a spectrally mixed state [15], as dictated by the biphoton's Schmidt mode structure. Therefore, interference of two such heralded photons, even with the same spectral mixture, does not produce high visibility because of their low spectral purity. Recent research in overcoming the low heralded-state spectral purity of SPDC outputs has been focused on methods of generating spectrally factorable biphoton state with an ideal Schmidt number of 1 [16, 17, 18, 19, 20, 21, 22, 23, 24, 25, 26]. A spectrally factorable biphoton state is frequency uncorrelated, and upon heralding, the signal photon has a well-defined and definite spectrum. By adopting the same generation method for all interacting photons, high-visibility interference measurements in photonic QIP tasks become achievable.

In this thesis, periodically-poled $KTiOPO_4$ (PPKTP) is the nonlinear crystal of choice for its type-II phase matching with outputs at telecom wavelengths. More importantly, PPKTP can be operated under extended phase matching [16, 27, 28] that allows the joint spectral amplitude (JSA) of the biphoton state to be controlled by

two independent parameters: the pump spectrum and the PPKTP phase-matching function. A previous experiment applied the extended phase-matching technique to a standard PPKTP crystal and obtained an ∼88% heralded-state purity without filtering [18]. It was pointed out that the standard sinc-function shape of the phase-matching function was the limiting factor for achieving higher purity, and that a Gaussian phase-matching function should in principle allow the purity to reach 100% without the need for spectral filtering. To fully optimize the biphoton state's heralded-state spectral purity, a PPKTP crystal was subsequently fabricated to yield a Gaussian-shaped phase-matching function [29], but no experimental characterization of its heralded-state purity was performed.

We employ the crystal design in [29] and fabricate a crystal with a longer length with an optimized Gaussian phase-matching function [30]. Theoretical analysis of the longer crystal shows a ∼99% achievable heralded-state purity without filtering. The major task in this master thesis work is to fully characterize the performance of the custom-fabricated Gaussian phase-matched crystal and verify a heralded-state purity of ∼99% as theoretically predicted. First, we perform a difference frequency generation measurement to ensure the phase-matching function has a Gaussian shape. Next, we characterize the joint distribution of the generated biphoton state by converting its spectral content to temporal information via a dispersion-based measurement. We also investigate two different configurations for the dispersion-based measurement. Previously, this is done using two long and equal-length fibers [19]. We implement two novel experimental configurations to achieve better performance: one that uses only one fiber and the other employs a low-loss dispersion compensation module. Finally, we test the indistinguishability of signal and idler photons by performing Hong-Ou-Mandel (HOM) interferometric measurements. Part of this thesis is published in [31].

1.2 Thesis Organization

This thesis studies several techniques for characterizing the generated biphoton state from a custom-fabricated Gaussian phase-matched PPKTP crystal. In chapter 2, we review the basics of the SPDC process. Standard phase-matching conditions and ex-

tended phase-matching conditions are reviewed. The joint spectral amplitude distributions of symmetric and asymmetric factorable SPDC biphoton states are discussed. We also review the calculation procedure of herald-state purity. Chapter 3 reviews the duty cycle modulation technique in fabricating the PPKTP crystal to yield its Gaussian-shape phase-matching function in periodically-poled crystals. The experimental verification of the Gaussian-shape phase-matching function is also discussed. Chapter 4 discusses the dispersion-based joint spectral density measurements of the SPDC biphoton output. The indistinguishability between signal and idler photons is studied in chapter 5. HOM interference and single-photon coherence time measurements are discussed in detail. Chapter 6 concludes this thesis and comments on possible future research.

Chapter 2

Extended Phase Matching Review

Spontaneous parametric down-conversion (SPDC) is a second order nonlinear process that converts a pump photon into a pair of signal and idler photons in a $\chi^{(2)}$ nonlinear crystal. The conversion process satisfies the phase-matching condition:

$$k_p = k_s + k_i, \tag{2.1}$$

and the energy conservation condition:

$$\omega_p = \omega_s + \omega_i, \tag{2.2}$$

where p, s, and i denote the pump, signal, and idler photons, respectively. $k_{p,s,i} \equiv \omega n_{p,s,i}(\omega)/c$ is the wave vector, which we write as scalar here by assuming collinear propagation for all three fields, even though in the general case the generated photons can be either collinear or noncollinear with respect to the pump beam. The SPDC process is said to be type-I, if the signal and idler photons have identical polarizations, or type-II, if they have orthogonal polarizations.

From Eq.(2.2), we see that the frequency sum of signal and idler photons is equal to the pump frequency. This condition also manifests that energy is conserved in this process. If ω_p is fixed, the signal and idler frequencies are anti-correlated. The signal and idler, however, are not monochromatic. Their center frequencies are set by the momentum conservation in Eq.(2.1) and their bandwidths are determined by the phase-matching function of the nonlinear crystal. Typically, any type of signal-

idler frequency correlation implies that the detection of signal photon projects the idler photon into a spectrally mixed state. In other words, frequency correlated biphotons cannot produce spectrally identical heralded photons. To obtain heralded pure-state photons, the frequency correlation between signal and idler photon needs to be eliminated. By imposing extended phase-matching conditions, which requires the group velocity mismatch to be zero in a nonlinear crystal, we are able to generate spectrally factorable biphoton state in which there is no frequency correlation between signal and idler. In this chapter, we start with reviewing the SPDC process under either monochromatic or pulsed pump. In section 2.3, we discuss how to achieve spectrally factorable state with an appropriate pump bandwidth. Finally, a review on calculating heralded-state purity is given.

2.1 Collinear SPDC with Monochromatic Light

If we consider the down-conversion event in a crystal with length L, we can write the biphoton output state as [28, 32]:

$$|\Psi\rangle = \int \frac{d\omega_s}{2\pi} \int \frac{d\omega_i}{2\pi} A(\omega_s, \omega_i) \hat{a}_s^\dagger(\omega_s) \hat{a}_i^\dagger(\omega_i) \, |0, 0\rangle \, , \tag{2.3}$$

where $A(\omega_s, \omega_i)$ is the frequency spectrum of the biphoton state. If we integrate the squared modulus of $A(\omega_s, \omega_i)$ over the frequency of one of the two modes, we obtain the fluorescence spectrum of the other mode. To get a better idea about the biphoton state, we will neglect the inconsequential normalization constants. Under the condition of collinear plane wave propagation of pump, signal, and idler photons, $A(\omega_s, \omega_i)$ can be written as [27, 28]:

$$A(\omega_s, \omega_i) = \alpha(\omega_s, \omega_i) \Phi_L(\omega_s, \omega_i), \tag{2.4}$$

$$\alpha(\omega_s, \omega_i) \equiv \frac{\sqrt{\omega_s \omega_i}}{n_s(\omega_s) n_i(\omega_i)} \xi_p(\omega_s + \omega_i), \tag{2.5}$$

where n_s and n_i are the refractive indices of the signal and idler modes in the nonlinear crystal, and the pump fluorescence spectrum, $|\xi_p(\omega)|^2$, is centered at ω_p and has a bandwidth Ω_p. The factors before $\xi_p(\omega)$ can in general be treated as constants over

the effective pump spectrum. And the phase matching function $\Phi_L(\omega_s, \omega_i)$ is:

$$\Phi_L(\omega_s, \omega_i) \equiv \frac{\sin[\triangle k(\omega_s, \omega_i)L/2]}{\triangle k(\omega_s, \omega_i)L/2}, \tag{2.6}$$

where $\triangle k$ is the phase mismatch defined as $\triangle k(\omega_s, \omega_i) = k_p(\omega_p) - k_s(\omega_s) - k_i(\omega_i)$. If the SPDC process is operating under the frequency degenerate condition, the center frequencies of signal and idler are the same and equal to half of the pump frequency. Because of the phase-matching conditions, the pump, signal, and idler indices have to obey:

$$n_p(\omega_p) = \frac{n_s(\omega_p/2) + n_i(\omega_p/2)}{2}. \tag{2.7}$$

We can then Taylor expand the phase mismatch $\triangle k$ in ω_s and ω_i around $w_p/2$, and obtain:

$$\triangle k(\omega_s, \omega_i) = (\omega_s - \omega_p/2)\gamma_s + (\omega_i - \omega_p/2)\gamma_i, \tag{2.8}$$

where $\gamma_s = k_p'(\omega_p) - k_s'(\omega_p/2)$, and $\gamma_i = k_p'(\omega_p) - k_i'(\omega_p/2)$. Note that k' denotes the derivative of k with respect to ω. With this result, and the newly defined variables $\tilde{\omega}_s = \omega_s - \omega_p/2$ and $\tilde{\omega}_i = \omega_i - \omega_p/2$, which represent the signal and idler frequency detunings from the degenerate frequency, the biphoton state in Eq.(2.3) can be expressed as:

$$\begin{aligned} |\Psi_{pm}\rangle = \int \frac{d\tilde{\omega}_s}{2\pi} \int \frac{d\tilde{\omega}_i}{2\pi} \alpha(\tilde{\omega}_s + \tilde{\omega}_i + \omega_p) \\ \frac{\sin[(\gamma_s\tilde{\omega}_s + \gamma_i\tilde{\omega}_i)L/2]}{(\gamma_s\tilde{\omega}_s + \gamma_i\tilde{\omega}_i)/2} \left|\omega_p/2 + \tilde{\omega}_s\right\rangle_s \left|\omega_p/2 + \tilde{\omega}_i\right\rangle_i . \end{aligned} \tag{2.9}$$

In the case where the pump beam is monochromatic, which is $\Omega_p \to 0$, $\alpha(\omega)$ becomes $\delta(\omega - \omega_p)$. Then the biphoton state becomes:

$$|TB\rangle = \int \frac{d\tilde{\omega}}{2\pi} \frac{\sin(2\pi\tilde{\omega}/\Omega_f)L}{2\pi\tilde{\omega}/\Omega_f} \left|\omega_p/2 + \tilde{\omega}\right\rangle_s \left|\omega_p/2 - \tilde{\omega}\right\rangle_i , \tag{2.10}$$

where $\Omega_f = \frac{4\pi}{L|\gamma_s - \gamma_i|}$ is the bandwidth of the fluorescence spectrum of signal and idler photons, and TB stands for twin-beam state. In the degenerate operating regime, signal and idler photons have the same spectra. However, this twin-beam state expression is valid only for type-II phase matching, since in type-I phase matching

an additional second order terms in Taylor expansion of the phase mismatch function $\triangle k$ is needed. This is because in the case of type-I phase matching, signal and idler photons have the same polarization and the first order expansion terms cancel [28]. For simplicity, we will only focus on the type-II phase matching case where Eq.(2.8) is valid.

From the biphoton bandwidth expression, $\Omega_f = \frac{4\pi}{L|\gamma_s - \gamma_i|}$, an increase of crystal length reduces the biphoton bandwidth. In the case where the crystal is infinitely long, the signal and idler photons have a very narrow bandwidth and can be considered essentially monochromatic. On the other hand, a longer crystal increases the down-conversion rate and yields a brighter entangled source.

As we can see in the twin-beam state expression, the frequencies of signal and idler photons are anti-correlated. In other words, if the frequency of signal photon ω_s is known, which may or may not equal to $\omega_p/2$, the frequency of idler photon is certain to be $\omega_p - \omega_s$. The sum of signal and idler frequencies is fixed and equal to the pump frequency. This twin-beam state is a maximally frequency entangled state. Therefore, the biphoton state is entangled in such a way that a frequency measurement of the signal photon will also determine the idler photon's frequency. Furthermore, the signal and idler photons are also correlated in time as they are always generated at the same time. This correlation, which exists both in frequency and time domains, exceeds the limit that classical physics permits. This is often called time-energy (or time-frequency) entanglement for the SPDC outputs, which has no correspondence in classical physics.

The assertion that signal and idler have identical spectra under degenerate operation holds for the case of a monochromatic pump laser, or when the pump bandwidth is small relative to the phase-matching bandwidth. For pump bandwidths that are comparable or larger than the phase-matching bandwidth, the two spectra do not usually match. If we consider a pump with a large bandwidth as made up of multiple monochromatic pumps, then the down-conversion process under most of the pumps are frequency-nondegenerate. The absence of signal and idler symmetry about the frequency-degenerate location (which is certainly true for type-II phase matching) implies that the two spectra are generally different. This is clearly shown experimentally for pulsed SPDC with a large pump bandwidth [33]. The distinguishability

in signal and idler spectra under broadband pumping is unfavorable to experiments or applications that rely on quantum interference, because quantum interference requires indistinguishable photons to yield high interference visibility [34]. In the next section, we discuss how to restore indistinguishability of signal and idler in the case of broadband pump.

2.2 Extended Phase-Matching Conditions

Under traditional type-II phase matching condition, the SPDC biphoton state is anti-correlated in frequency. Using Eq.(2.8), we can express the phase-matching function in terms of the inverse of group velocities γ_s and γ_i. If we express the two variables in polar coordinates, we have $\gamma_s = \gamma\cos(\theta)$ and $\gamma_i = \gamma\sin(\theta)$. The parameter γ controls the width of the phase matching function Φ_L and therefore determines the biphoton bandwidth. The parameter θ controls the symmetry axis $\tilde{\omega}_i = -\tilde{\omega}_s\tan(\theta)$ of the phase matching function Φ_L and therefore determines the structure of the biphoton spectrum. By manipulating the variable θ, we can effectively control the frequency correlation between the signal and idler photons [28].

In order to produce the spectrally indistinguishable signal and idler photons with positive frequency correlation, we want the biphoton spectrum $A(\omega_s, \omega_i)$ to be symmetric with respect to ω_s and ω_i. For type-II phase matching, this condition can be achieved when $\gamma_s = \gamma_i$ and $\theta = \frac{\pi}{4}$. This imposes an additional requirement, which is the group velocity matching condition:

$$k_p'(\omega_p) = \frac{k_s'(\omega_p/2) + k_i'(\omega_p/2)}{2}. \tag{2.11}$$

When both Eq.(2.7) and Eq.(2.11) are satisfied, the biphoton state is phase matched over the entire pump fluorescence spectrum. Together they are known as the extended phase matching conditions [28]. If both conditions are satisfied, the biphoton spectral amplitude is of the form: $A(\omega_s, \omega_i) = \alpha(\omega_s+\omega_i)\Phi(\omega_s-\omega_i)$, which means α is a function of $\omega_s + \omega_i$ and Φ is a function of $\omega_s - \omega_i$. The symmetry axis of the pump spectral function $\alpha(\omega_s + \omega_i)$, which has a θ value of $\pi/4$, is perpendicular to the symmetry axis of the phase-matching function, which has a θ value of $-\pi/4$. Comparisons of

the biphoton spectral amplitude $|A(\omega_s, \omega_i)|$ in both traditional phase matched and extended phase matched cases are shown graphically in Fig. 2-1. We note that when the group velocity condition in Eq. (2.11) is not satisfied, the phase-matching function does not have a requirement for any particular θ value.

Under extended phase-matching conditions, the biphoton state becomes:

$$|\Psi_{epm}\rangle = \int \frac{d\tilde{\omega}_s}{2\pi} \int \frac{d\tilde{\omega}_i}{2\pi} \alpha(\tilde{\omega}_s + \tilde{\omega}_i + \omega_p) \\ \frac{\sin[\pi(\tilde{\omega}_s - \tilde{\omega}_i)/\Omega_f]L}{\pi(\tilde{\omega}_s - \tilde{\omega}_i)/\Omega_f} \left|\omega_p/2 + \tilde{\omega}_s,\right\rangle_s \left|\omega_p/2 + \tilde{\omega}_i,\right\rangle_i . \tag{2.12}$$

If the pump is broadband and the crystal is infinitely long, $L \to \infty$, we can write the difference beam state in which the signal and idler frequencies are the same:

$$|DB\rangle = \int \frac{d\tilde{\omega}}{2\pi} \alpha(2\tilde{\omega} + \omega_p) \left|\omega_p/2 + \tilde{\omega}\right\rangle_s \left|\omega_p/2 + \tilde{\omega}\right\rangle_i . \tag{2.13}$$

Compare to the $|TB\rangle$ state, the biphoton spectrum of $|DB\rangle$ state is completely determined by the pump spectral characteristics. If we look at both states from a Fourier optics standpoint, the properties of $|TB\rangle$ and $|DB\rangle$ states are complimentary of each other. If the crystal is pumped by a cw laser, the average time needed for the generated photons to travel across the crystal ($\sim L/c$) is much smaller than the laser coherence time. Furthermore, the two photons generated in this $|TB\rangle$ state are time correlated, and by Fourier duality, they are frequency anti-correlated. On the contrary, in the $|DB\rangle$ state, although the two photons are generated together, the two photons see different indices and travel at different speeds. However, the group velocity matching condition guarantees that the mean position of the two photons is always centered at the pump pulse location. Therefore, they are time anti-correlated and frequency correlated. This idea is illustrated in Fig.2-2. An important thing to note is that although the two photons are frequency correlated, it does not violate energy conservation. The understanding of this counter-intuitive phenomenon is that these photons are generated by a broadband pulse, which has many frequency components, and the photons can be generated with respect to any frequency components within the pulse.

For the case of a monochromatic pump, $\Omega_p \to 0$, we again obtain the twin beam

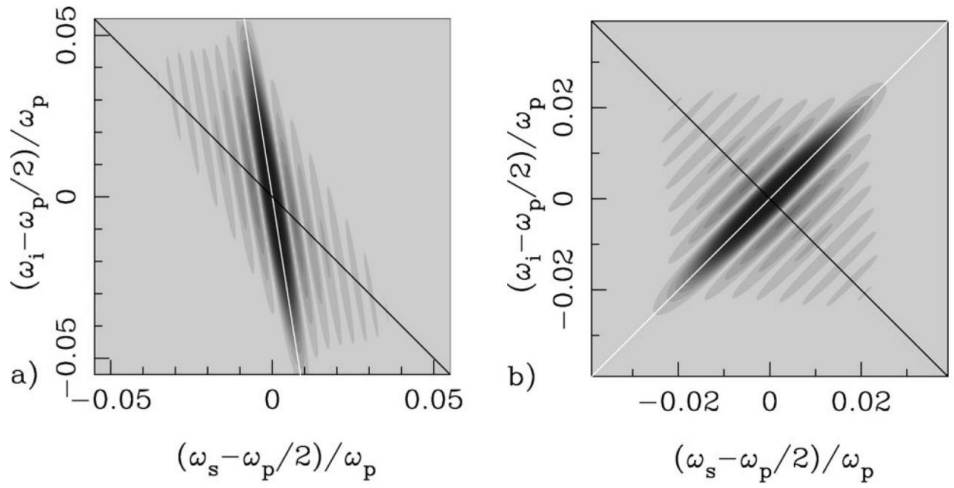

Figure 2-1: Plots of $|A(\omega_s, \omega_i)|$ of crystal length L and pump bandwidth Ω_p (reproduced from [28]). In each plot the white line is the symmetry axis of $\Phi_L(\omega_S, \omega_i)$ and the black line is the symmetry axis of $\alpha(\omega_S+\omega_i)$, which is chosen assuming a Gaussian pump spectrum $exp[-(\omega-\omega_p)^2/\Omega_p^2]$. (a) Only standard phase-matching condition is satisfied. The two symmetry axes are not orthogonal but at an angle determined by the nonlinear crystal used (The parameters used for plotting are $\theta = \pi/20$, $L = 1$ cm, and $\Omega_p = 4 \times 10^{13}$ s^{-1}). (b) Extended phase-matching conditions are satisfied. The two symmetry axes are orthogonal (The parameters used for plotting are $\theta = -\pi/4$, $L = 1$ cm, and $\Omega_p = 4 \times 10^{13}$ s^{-1}).

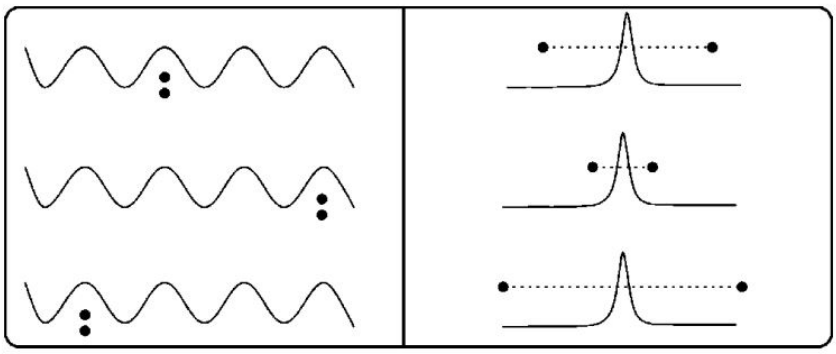

Figure 2-2: Time domain pictorial representation of parametric down-conversion (reproduced from [28]). The signal and idler photons are created simultaneously within a coherence time of time inside the crystal. The $|TB\rangle$ state is shown on the left, where the crystal is pumped by a cw pump. The two photons are shown as two dots. The two photons are *time correlated* and *frequency anti-correlated*. The $|DB\rangle$ state is shown on the right, where the crystal is pumped by a pulsed pump. The two photons are *time anti-correlated* and *frequency correlated*.

state $|TB\rangle$ from $|\Psi_{epm}\rangle$. Therefore this extended phase matching is the same as the standard phase matching if the crystal is cw pumped. Furthermore, both $|\Psi_{pm}\rangle$ and $|\Psi_{epm}\rangle$ depend on the particular shape of the pump bandwidth Ω_p and the biphoton spectrum Ω_f, which depends on the phase-matching function of the nonlinear crystal. By controlling these two parameters, we can manipulate the output spectrum of the biphoton state. In the case where the crystal length is finite, the condition that yields a maximally entangled state no longer holds. However, the positive frequency correlation between signal and idler are intact, and their spectra remain the same. Therefore, the indistinguishability is preserved when the pump has a large bandwidth and high visibility in Hong-Ou-Mandel (HOM) type quantum interference experiments for all values of pump bandwidth can still be observed [35].

If the second order contributions of the Taylor expansion of the phase mismatch function $\triangle k$ cannot be neglected, for instance, in the case of type-I phase matching, we can still achieve the extended phase-matching condition and obtain a frequency correlated state. In addition to Eq. (2.7) and Eq. (2.11), we will need the second order terms to satisfy:

$$k_s''(\omega_p/2) = k_i''(\omega_p/2) = 2k_p''(\omega_p). \tag{2.14}$$

If contributions of higher order are presented, the above requirement can be extended to:

$$\frac{\partial^n k_p}{\partial \omega^n}(\omega_p) = \frac{1}{2^n}[\frac{\partial^n k_s}{\partial \omega^n}(\omega_p/2) + \frac{\partial^n k_i}{\partial \omega^n}(\omega_p/2)]. \tag{2.15}$$

However, in reality, it is hard to find a material that satisfies this extended phase-matching condition. This is because the extended phase-matching condition requires the group velocity of one of the generated photon to be smaller than the group velocity of the pump, which has a shorter wavelength. Nonetheless, we can utilize the quasi-phase-matching technique to satisfy the tradition phase-matching condition shown in Eq. (2.7). Finally, we should note that extended phase matching is called the zero group-velocity mismatch regime in ultrafast optics.

2.3 Factorable Biphoton JSA

A spectrally factorable biphoton state can be formed typically with one of two possible JSA profiles, an asymmetric configuration or a symmetric configuration. The asymmetric JSA [36, 37] has an elongated profile (like a long rectangle) with the long side oriented along the idler (ω_i) frequency axis. This is often achieved in a periodically-poled KD_2PO_4 (KDP) crystal, where the extended phase-matching conditions are satisfied when the pump beam is propagating at an angle of 67.8° to the optical axis. Furthermore, the pump (extraordinary beam) is set to be 415 nm and the generated signal and idler (ordinary beam) are both centered at 830 nm, in which wavelength range where high-efficiency silicon avalanche photodiodes (APDs) are available. In this asymmetric configuration, detecting the idler photon yields a signal (ω_s) photon in a narrow single frequency mode, regardless of the idler frequency measurement. The asymmetric JSA has been demonstrated [17] showing good results that agree with theoretical predictions.

The second JSA profile for a factorable biphoton has a circularly symmetric shape and is based on extended phase-matching in which the JSA is the product of the pump spectrum at $(\omega_s + \omega_i)$ and the crystal phase-matching function that can be approximated by a $(\omega_s - \omega_i)$ dependence for a reasonably long crystal with type-II phase matching [28, 37, 38]. The pump and phase-matching parameters are oriented at $+45°$ and $-45°$ with ω_s and ω_i axes so that the controls using $\omega_s \pm \omega_i$ parameters allow for orthogonal and convenient adjustments of the JSA. This approach follows the extended phase-matching technique that has been applied successfully in a number of experiments [18, 19, 21, 22, 23, 24, 25, 26, 39, 40]. The extended phase matching condition is satisfied by periodically poled $KTiOPO_4$ at a pump wavelength of 791 nm with a grating period of 46.1 μm when propagation is along the crystal's X axis. The pump and idler photons are Y polarized (ordinary beam), and the signal photon is Z polarized (extraordinary beam) [41].

When we multiply the pump spectrum intensity and the phase-matching function intensity, we obtain the biphoton joint spectral density (JSD) profile. Taking the square-root of the JSD gives us the JSA, assuming that the biphoton state has a flat phase. Both JSD profiles obtained from asymmetric and symmetric configurations

are shown in Figure 2-3.

Both configurations for achieving factorable JSA are equally valid. In order to use many existing technologies in the telecommunication wavelength, this thesis focuses on the symmetric configuration where the generated signal and idler are both in the telecommunication wavelength. Furthermore, the symmetric configuration gives orthogonal control of the JSA via pump envelope and phase-matching function, which are used to design a circularly symmetric JSA.

2.4 Biphoton Heralded-state Purity

Frequency correlation between signal and idler photons is undesirable in the heralded generation of pure-state single photons. To quantify the correlation that exists between the signal and idler photons, we need to perform Schmidt decomposition [13] on the biphoton wavefunction in two orthonormal bases denoted as $|\psi_n^s\rangle$ and $|\psi_n^i\rangle$. Therefore, the biphoton wavefunction in Eq. (2.3) can be written as [42]:

$$|\Psi\rangle = \sum_n \sqrt{\lambda_n}\, |\psi_n^s\rangle\, |\psi_n^i\rangle\,, \tag{2.16}$$

with $\sum_n \lambda_n = 1$. The purity of the heralded photon state can be derived from the biphoton state. For instance, if the idler photon is detected, the signal photon state can be calculated using the reduced density operator:

$$\hat{\rho}_s = Tr_i(|\Psi\rangle\langle\Psi|) = \sum_n \lambda_n\, |\psi_n^s\rangle\langle\psi_n^s|\,. \tag{2.17}$$

The purity of the heralded signal photon is given by:

$$P_s = Tr(\hat{\rho}_s^2) = \sum_n \lambda_n^2 = \frac{1}{K}, \tag{2.18}$$

where K is the Schmidt number defined as $K = 1/\sum_n \lambda_n^2$. If $K = 1$, the biphoton state can be written as the product of a signal photon state and an idler photon state. In this case, the signal and idler are uncorrelated in frequency and can be treated individually. If $K > 1$, the biphoton state cannot be written as the product of signal

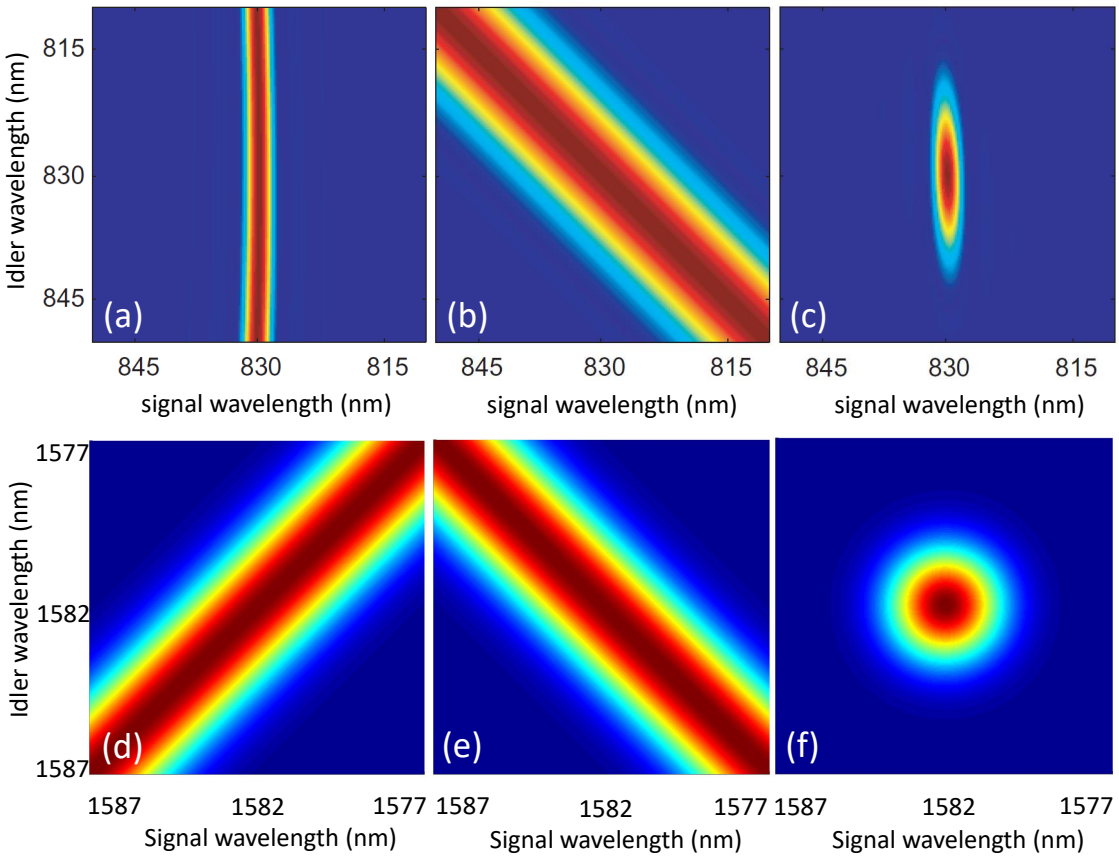

Figure 2-3: Simulation of factorable biphoton state JSD. Asymmetric configuration (plots reproduced from [37]):(a) PPKDP phase-matching function intensity, (b) pump envelope spectrum intensity, (c) joint spectral density of signal and idler photons. Symmetric configuration:(d) PPKTP phase-matching function intensity, (e) pump envelope spectrum intensity, (f) joint spectral density of signal and idler photons. Both JSD profiles result in a factorable biphoton state where signal and idler photons are independent of each other.

and idler states. A larger K value indicates a stronger correlation.

However, it is not easy to calculate K based on the measured joint spectral density data, because there may not be an analytic method of finding the Schmidt number for a general set of biphoton states. Therefore, an alternative method is needed to decompose the joint spectrum information into the density matrix form. This method is known as single value decomposition (SVD) which can be used to calculate the purity from any arbitrary joint intensity [37]. Define a square matrix F for the measured state $|\Psi\rangle$, where F_{mn} is the matrix element representing $A(\omega_{m,s}, \omega_{n,i})$ and $\omega_{m,s}$ and $\omega_{n,i}$ are the discrete frequency components of signal and idler photons, respectively. The SVD of F is defined as the decomposition of F into two unitary matrices, U and $V^\dagger$, and a diagonal matrix, D, such that:

$$F = UDV^\dagger. \tag{2.19}$$

The unitary matrices contain the modes into which the measured state has been decomposed. U depends only on ω_s and its jth column, U_{mj} represents the signal photon Schmidt mode $|\psi_j^s\rangle$. Similarly, $V^\dagger$ depends only on ω_i and its jth row, and $V_{jm}^\dagger$ describes the idler photon Schmidt mode $|\psi_j^i\rangle$. The diagonal elements of D are the singular values of F, which are non-negative and appear in descending order. If the initial state $|\Psi\rangle$ is normalized, the singular values are identical to the Schmidt magnitudes. Therefore, the trace of matrix D gives us the purity of the heralded photons. This method can be evaluated numerically efficiently even for relatively large matrices. It is extremely useful for a biphoton state where there is no analytic solution for its Schmidt decomposition.

Chapter 3

Spectral Engineering of Phase-Matching Function

In an earlier experimental attempt to generate biphotons with high heralded-state spectral purity by SPDC under extended phase-matching conditions, a purity of 88% was obtained without any spectral filtering [18]. It was pointed out that the standard sinc-function shape of the phase-matching function was the limiting factor, and that a Gaussian phase-matching function should in principle allow the (spectrally unfiltered) purity to reach 100%. The limitation of the sinc-function shape stems from the presence of its side lobes that break the circular symmetry of the JSA profile. Later experiments that also utilized extended phase matching show similar purity measurement results [21, 22, 23, 25, 26, 40]. Generally, spectral filtering is undesirable partly because of insertion loss due to the filters. In addition, when we consider interference between independent heralded single photons from different sources, it can be difficult to match the spectral shapes of the different filters used to eliminate all the side lobes while passing a Gaussian-shaped main lobe of the sinc-shaped phase-matching function. More problematic is the uncertainty of the relative temporal positions of the heralded photons. Because the unfiltered biphoton state has a Schmidt number greater than 1, the heralded single photon is in a mixed state of two or more eigenstates that may have different temporal locations. Spectral filtering of the biphotons' signals and idlers does not affect their relative temporal locations such that interference measurements which require precise timing of the independent

photons are degraded.

A better way than spectral filtering the outputs is to modify the ferroelectric domain structure of the periodically-poled nonlinear crystal to yield a phase-matching function that has a Gaussian shape instead of the usual sinc-function shape. In standard crystals, the domains are aligned in the same direction, whereas in periodically-poled crystals the domains are alternately aligned and oppositely-aligned with a 50:50 duty cycle, each occupying half of a poling period Λ.

Two methods have been proposed and demonstrated for realizing a Gaussian phase-matching function. One is to change the poling period along the length of the crystal, with periods equal to integer multiples of Λ and with the duty cycle remaining at 50:50 [43]. The higher order periods yield lower effective nonlinearity that can be used to tailor the phase-matching function to have a Gaussian shape. The second method keeps the poling period at Λ but varies the duty cycle along the length of the crystal which also lowers the effective nonlinearity [29]. Both methods are expected to achieve similar results in purity measurements of $\sim$97% without any filtering and greater than 99% with a mild spectral filter to further suppress the residual side lobes. In this chapter, we first review the second method of modifying the duty cycle along the length of the crystal, which is described in detail in [29]. With some optimizations of the custom grating structure, we fabricated a PPKTP crystal which has an achievable heralded-state spectral purity of $\sim$99% without filtering [30]. Finally, in Sec. 3.2, we show the measurement result of the phase-matching function of the custom-fabricated crystal.

3.1 Modification of Grating Structure

In quasi-phase matching, the phase-matching function $G(\triangle k)$ is given by [29, 44]:

$$G(\triangle k) = \frac{1}{L}\int_0^L g(z)exp(-i\triangle kz)dz, \tag{3.1}$$

where $g(z) = d(z)/d_{eff}$ is the signed fractional nonlinear coefficient whose value is either $+1$ or -1, d_{eff} is the effective nonlinearity of the nonlinear crystal, and $\triangle k$ is the wave number mismatch. $g(z)$ is 1 for one polarization of the ferroelectric domain,

and -1 for the opposite polarization. In the first order poling case, the alternating equal length segments of $g(z) = 1$ and $g(z) = -1$ within each grating period Λ yields the maximum efficiency.

From Eq. (3.1), we see that $G(z)$ and $g(z)$ are a Fourier transform pair. Therefore, the phase-matching function $G(z)$ can be modified by changing $g(z)$. Given that $g(z)$ is constant within each ferroelectric domain segment and it changes sign across the poling boundary, we can express $g(z)$ as:

$$g(z) = \sum_{j=0}^{N} (-1)^j [H(z - z_j) - H(z - z_{j+1})], \tag{3.2}$$

where N is the number of domain segments with $z_0 = 0$ and $z_{N+1} = L$, z_j is the j^{th} poling boundary, and $H(z)$ is the unit step function. Therefore, the phase matching function can be evaluated using:

$$\begin{aligned} G(\triangle k) = \; & \frac{2}{\triangle k L} \sum_{j=0}^{N} (-1)^j \sin[\frac{\triangle k (z_{j+1} - z_j)}{2}] \\ & \times \exp[\frac{-i \triangle k (z_{j+1} + z_j)}{2}]. \end{aligned} \tag{3.3}$$

From Eq. (3.3), we can calculate the desired grating period $\Lambda \equiv 2(z_{j+1} - z_j) = \frac{2\pi}{\triangle k_c}$, where $\triangle k_c$ is the wave vector mismatch at the center operating wavelength. The Fourier transform of a Gaussian function is also a Gaussian. Therefore, if we want the phase matching function $G(z)$ to be Gaussian, we need the function $g(z)$ to be a Gaussian as well. The above equation suggests that this is achievable via manipulating the poling boundaries z_j. In this approach, we hold the spacing between the even numbered boundaries to be constant at the fixed grating period $\Lambda = \frac{2\pi}{\triangle k_c}$, while changing the odd numbered boundaries with $z_{2j+1} = (j + r_j)\Lambda$. r_j is the duty cycle and is defined to be $0 \leq r_j \leq 1$. Therefore, specific duty cycle can be selected through numerical calculation so that the phase matching function $G(k)$ approximates a Gaussian.

To operate under extended phase matching and therefore to achieve the group velocity matching condition in Eq. (2.11), we chose periodically-poled KTP with a broadband pump centered at 791 nm and a degenerate output wavelength of 1582

nm. Our PPKTP crystal was 18 mm long with a poling period $\Lambda = 46.1$ μm chosen to yield type-II phase-matched outputs. In the custom-fabricated PPKTP we designed the crystal with the duty cycle $r(z)$, which was calculated numerically from a Gaussian function, ranging from a ratio of 10:90 to 90:10 [30]. The crystal was anti-reflection coated at both 791 and 1582 nm wavelengths.

3.2 Phase-matching Function Measurement

Efficient three-wave mixing process only occurs if the three waves are phase-matched inside a nonlinear crystal. In principle, we can express the three-wave mixing signal as a function of the phase-matching function. For a nondepleted pump and laser probe input, the amplitude of the generated difference frequency signal is:

$$E_3 = 0.62 * \frac{-i\omega_3 E_1 E_2^*}{n_3 c} d_{eff} L G_{norm}(\triangle k), \tag{3.4}$$

where this equation is obtained from coupled-mode equations for a difference frequency generation (DFG) process and $G_{norm}(\triangle k)$ is the normalized phase-matching function $G(\triangle k)$ for a periodically poled crystal with a 50:50 duty cycle. The factor 0.62 is the expected reduction in nonlinearity due to the Gaussian poling pattern [29]. The input pump is E_1 with a fixed frequency ω_1 and the probe beam is E_2 with a tunable frequency ω_2. L is the crystal length, n_j is the index of refraction for the corresponding electric field E_j, and $\triangle k = k_1 - k_2 - k_3$ is wave vector mismatch inside the crystal with all beams collinearly propagated.

3.2.1 Experiment Setup and Results

To obtain the DFG signal, a continuous-wave pump at 791 nm with ∼100 mW of power was combined with a tunable ∼3-mW probe laser centered at 1582 nm to serve as inputs to the PPKTP crystal. The crystal was type-II phase-matched and both inputs propagated along the crystal x-axis. The pump laser was horizontally polarized along the crystal's y-axis and the probe laser was vertically polarized along the crystal's z-axis. The pump was focused onto the center of the crystal with a beam waist of 50 μm, and the probe was focused to a beam waist of 60 μm. We note that

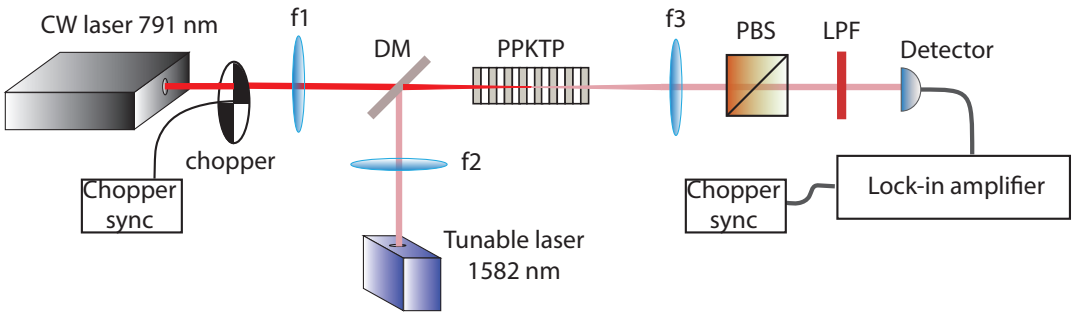

Figure 3-1: Schematic of DFG measurement setup. DM, dichroic mirror; f1 = 20 cm; f2 = 13 cm; f3 = 10 cm; PBS, polarization beam splitter; LPF, long-pass filter.

this is not the optimal probe focus beam waist. The optimally focused probe beam should have a beam waist of 71 μm. The DFG signal was horizontally polarized with a frequency given by the frequency difference between the pump and probe inputs. A polarization beam splitter and a long-pass filter were used to remove the vertically-polarized probe and the 791-nm pump. The leftover DFG signal was focused onto a low-noise InGaAs photodetector (Thorlabs model PDA-255). The output of the photodetector was sent to a lock-in amplifier that was synchronized to the pump chopping frequency at 600 Hz. A schematic of this measurement setup is shown in Fig. 3-1.

The crystal's temperature was maintained at 26.4°C so that the peak DFG output occurred at the probe wavelength of 1582 nm, or twice the pump wavelength. The probe laser wavelength was scanned and the DFG signal was recorded, as shown in Fig. 3-2 in linear scale and Fig. 3-3 in log scale. The measurements show a significant reduction in the usual sinc-function side lobes and a phase-matching function that is Gaussian to a large extent. Figure 3-3 shows a weak sideband signal at 1578 nm that we believe is mostly caused by noise in our measurement system. As we will see in Chapter 4, the side lobe suppression can be measured to be much better than that shown in Fig. 3-3. With 100 mW pump and 2.5 mW probe inputs, 27 nW DFG signal was detected. Using Eq. (3.4), we found the d_{eff} of the PPKTP crystal used to be 2.06 pm/V. We note that custom duty-cycle modulated crystal experiences a 38% decrease in effective nonlinearity compare to standard uniformly poled crystal. This factor was taken into consideration when d_{eff} was calculated.

A major contribution to the background noise was from the residual probe light.

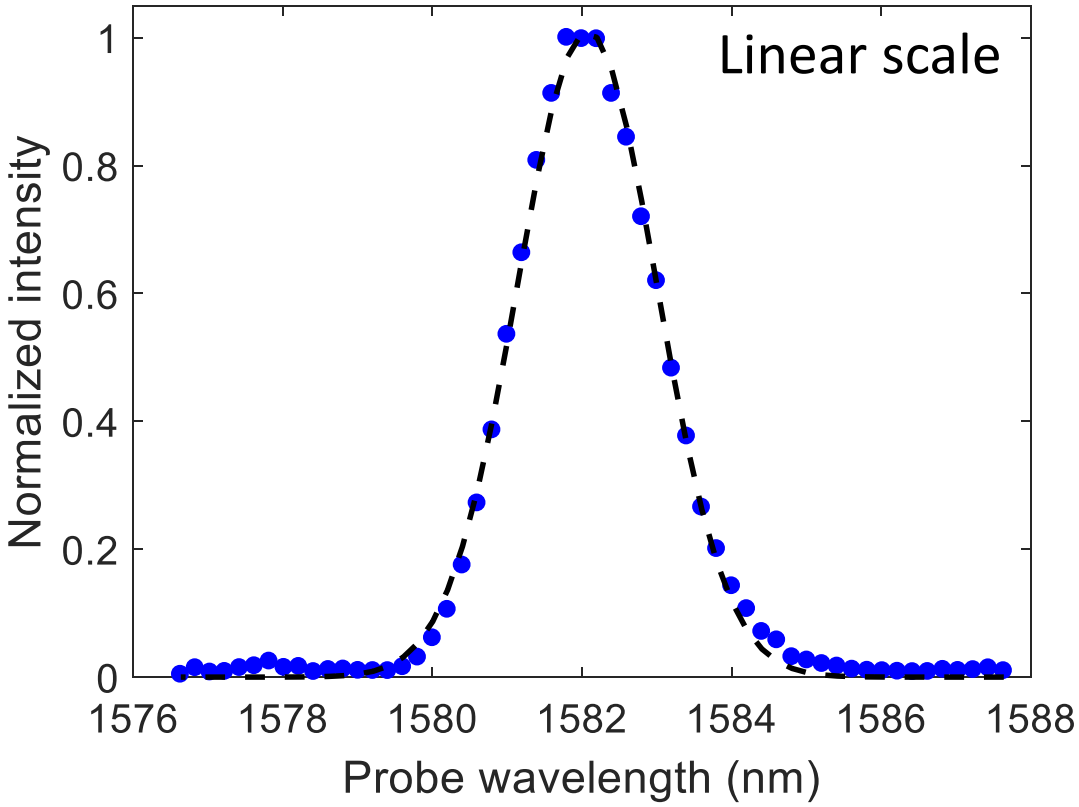

Figure 3-2: Difference-frequency generation outputs as a function of the probe wavelength to confirm Gaussian-shaped phase-matching function based on duty-cycle modulation [29, 30] in linear scale. DFG outputs are normalized to the peak value. The blue dots are measured data and the black dashed line denotes the fitted Gaussian curve.

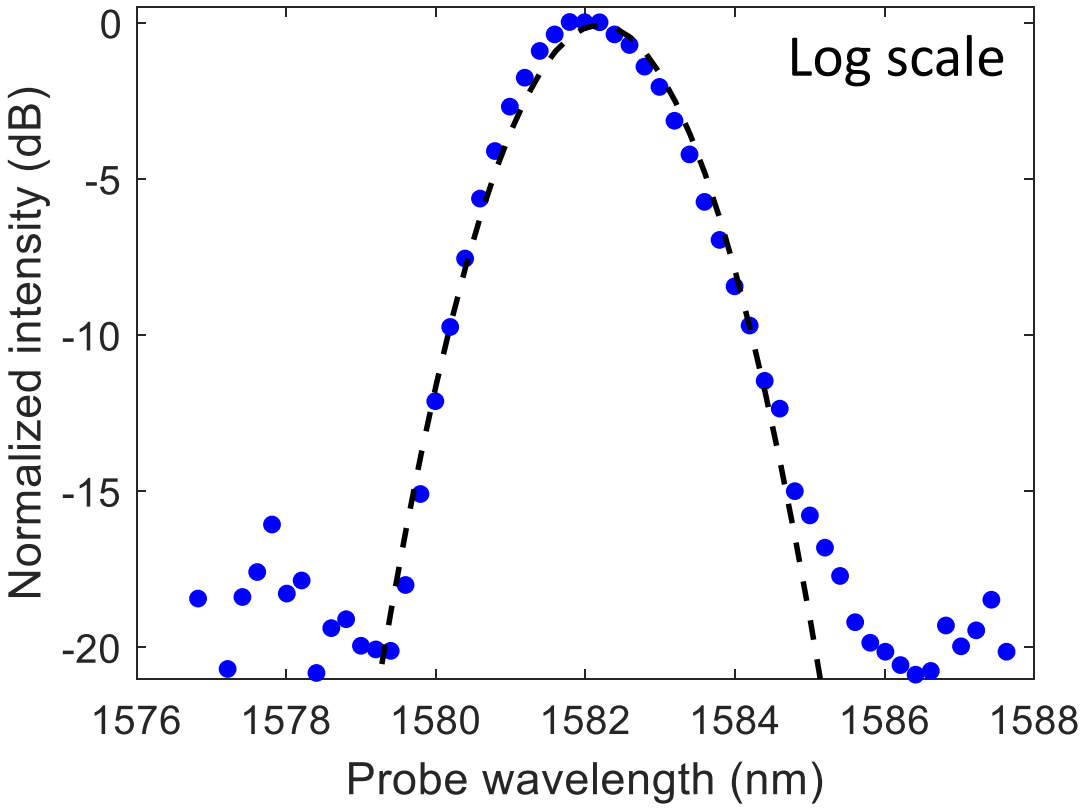

Figure 3-3: Difference-frequency generation outputs as a function of the probe wavelength to confirm Gaussian-shaped phase-matching function based on duty-cycle modulation [29, 30] in log scale. DFG outputs are normalized to the peak value. The blue dots are measured data and the black dashed line denotes the fitted Gaussian curve.

The polarization beam splitter in the setup had a finite extinction ratio at 30 dB and was not able to eliminate the probe beam completely. Furthermore, as the probe laser wavelength was tuned, its output experienced a slight polarization drift, which also contributed to a higher background noise. The signal to noise ratio of this experiment could be further improved if a higher extinction ratio polarization beam splitter, or two standard polarization beam splitters were used. The improvement on eliminating probe beam would result in a lower background noise.

3.2.2 Alignment Procedure

The alignment of this three-wave mixing experiment is tricky. This section describes the alignment and output signal optimization procedures. The main difficulty is overlapping the pump beam and the probe beam. One way for overlapping them is to pass both of them through two widely separated pinholes placed along the propagation path. Before we put the crystal and lenses in the setup, we fixed the pump beam path and recorded its beam path using two pinholes that were placed before and after the intended crystal location. The two pinholes should be placed as far apart as possible to make the alignment more precise. Once the pump beam path was set and all mounts were securely fastened, we could start the overlapping process. We used two mirrors to steer the probe beam until the two beams were overlapped at both pinhole locations.

Focusing lenses were then put into the pump and probe beam paths. A Thorlabs beam profiler was used to check their minimum beam waist locations and to make sure that they were the same. After the lenses were put in, the two beams should still overlap at both pinhole locations. We then positioned the crystal so that the foci of the pump and probe beams were at the crystal center. The pump or the probe beam might move slightly during this process. However, they should still overlap. Then we could see the DFG signal after the pump and probe were filtered. If no signal was detected, then the overlapping of the pump and probe beams was not good enough. One could try to redo the alignment procedure with the two pinholes placed further apart.

If the pump beam was not completely filtered, it could also be picked up by the lock-in detection because the pump was modulated at the same chopping frequency.

To determine if it was the real DFG signal, one could turn off the probe laser. If there was still signal from the detector, then it was not the real DFG signal. If the DFG signal was confirmed to be real, we could then walk either the pump or the probe beam, but not both, to improve the beam overlap and to maximize the detected DFG signal.

Chapter 4

Biphoton Joint Spectral Density

To quantify the spectral purity of the SPDC output, one can measure the signal-idler joint spectral density distribution and apply the Schmidt decomposition procedure shown in Section 2.4 to calculate the heralded-state purity of the biphoton state, assuming that the state is transform limited. The most common method of making JSD measurements is to send the pulsed SPDC outputs through two equal-length optical fibers, one for signal and the other for idler, to disperse them before measurement by time-correlated coincidence detection. Fiber dispersion serves to perform frequency-to-time conversion and allows one to easily measure the frequency correlation of photon pairs based on their arrival times [45]. The resolution of the fiber spectrometer depends on the length of the fibers and the timing resolution of the single-photon detectors. A typical setting with 20 km of standard single-mode fibers (dispersion coefficient of ∼17 ps/nm/km) and superconducting nanowire single-photon detectors (SNSPDs) with a timing resolution of 100 ps yields a spectral resolution of 0.3 nm. To obtain a higher spectral resolution requires longer fibers with the drawback that the coincidence detection rate is reduced by the combined insertion loss of the two fibers (∼0.2 dB/km at telecom wavelengths). To reach 0.12 nm resolution requires 50 km of fiber that reduces the coincidence detection rate by a factor of 100 when compared with the detection rate without the fibers. In practice the two individual fibers should be of the same length and temperature stabilized to avoid timing errors caused by their relative length change.

Our approach to JSD characterization aims to simplify the measurement setup and

to obtain enhanced performance. Two configurations are utilized: one uses a single optical fiber with counter-propagating beams to ensure signal and idler see the same fiber length and dispersion, and the second one employs a commercially available low-loss dispersion compensation module to achieve higher resolution without sacrificing coincidence detection rates.

4.1 Generation of SPDC photon pairs

4.1.1 Experiment Setup

The SPDC pump laser was an 80-MHz mode-locked, horizontally-polarized, ∼100 fs Ti-sapphire laser centered at 791 nm. The optical bandwidth of the pump is one of the parameters for controlling the SPDC biphoton output. To modify the pump bandwidth we implemented a linear spectral filtering system using a pair of identical diffraction gratings (Richardson Gratings 53-*-230H) in a $4f$ dispersion-free optical configuration [46, 47]. Two identical lenses L1 with focal length $f = 20$ cm were placed $2f$ apart, and the two diffraction gratings were located a distance f from the lenses, as shown in Fig. 4-1(a). The first grating dispersed the collimated pump beam spectrally and the first lens focused the spectrally dispersed components at the focal plane located at a distance f from L1. We placed an adjustable rectangular aperture at the focal plane to control the transmission of the parallel spectral components and therefore the bandwidth of the transmitted pump. The second lens and second grating recombined the transmitted spectral components into one collimated beam with the desired bandwidth. With the aperture wide open, the output of the $4f$ system had the same spectrum as the input's.

We focused the pump to a beam waist of ∼124 μm at the center of the PPKTP crystal that was temperature stabilized at 26.4 ± 0.1°C to yield wavelength degenerate signal and idler outputs at 1582 nm. The orthogonally polarized signal and idler were coupled into a single-mode polarization-maintaining (PM) fiber with beam collection optics designed to optimize the symmetric heralding efficiency in single-mode fiber coupling [48, 49]. As shown in Fig. 4-1(a) the pump was rejected before fiber coupling by a long-pass filter with a cutoff wavelength of 1300 nm, and the signal and idler

polarizations were aligned with the PM fiber's fast and slow axes using the combination of a quarter-wave plate and a half-wave plate. For a pump bandwidth of 5.6 nm and at a pump power of 27 mW, we measured singles of ∼95,800/s and ∼108,000/s, and ∼30,000 coincidences/s, which yields an average system efficiency of ∼29%. The system efficiency is determined by the following factors: detector efficiency, optical components losses, fiber coupling efficiency, and the single-mode coupling efficiency. In our experiment, the detector efficiency was measured to be $\sim 80\%$, and the optical components losses were measured to be $\sim 77\%$. The single-mode coupling efficiency was then found to be $\sim 50\%$.

Detector efficiency and losses from optical components can be improved by getting more efficient detectors and lower loss optical hardware. The fiber coupling efficiency can be improved by matching the input and coupled spatial modes. The single-mode coupling efficiency, however, is the intrinsic source efficiency that can only be optimized by setting appropriate pump and collection beam waists. The single-mode coupling efficiency is defined as the probability of the idler photon being coupled into a single-mode fiber, given that signal photon is coupled into the same fiber. To have a higher single-mode coupling efficiency, the pump should be loosely focused. A theoretical model predicting heralding efficiency based on pump and collection beam waists can be found in [48, 49]. However, because a loosely-focused pump generates more modes and the total number of generated signal and idler pairs is proportional to the pump power, the pair generation rate at a particular collection mode decreases as the pump gets focused more loosely. Proper pump focusing beam waist and collection beam waist should be chosen depending on the specific application.

4.1.2 Alignment Procedure

Once the desired focusing beam waist and the collection beam waist were known, we used a back-propagation technique to align the system. We sent a 1582-nm fiber coupld laser beam from the fiber to back-propagate towards the pump laser. By overlapping the 791-nm pump and the 1582-nm beam with pinholes, we successfully coupled the pump beam into the fiber. Because of mode mismatch, the fiber would not be able to collect much pump light, but the power was still sufficient to be detected by a regular fiber-coupled InGaAs detector. Once the pump beam was detected in

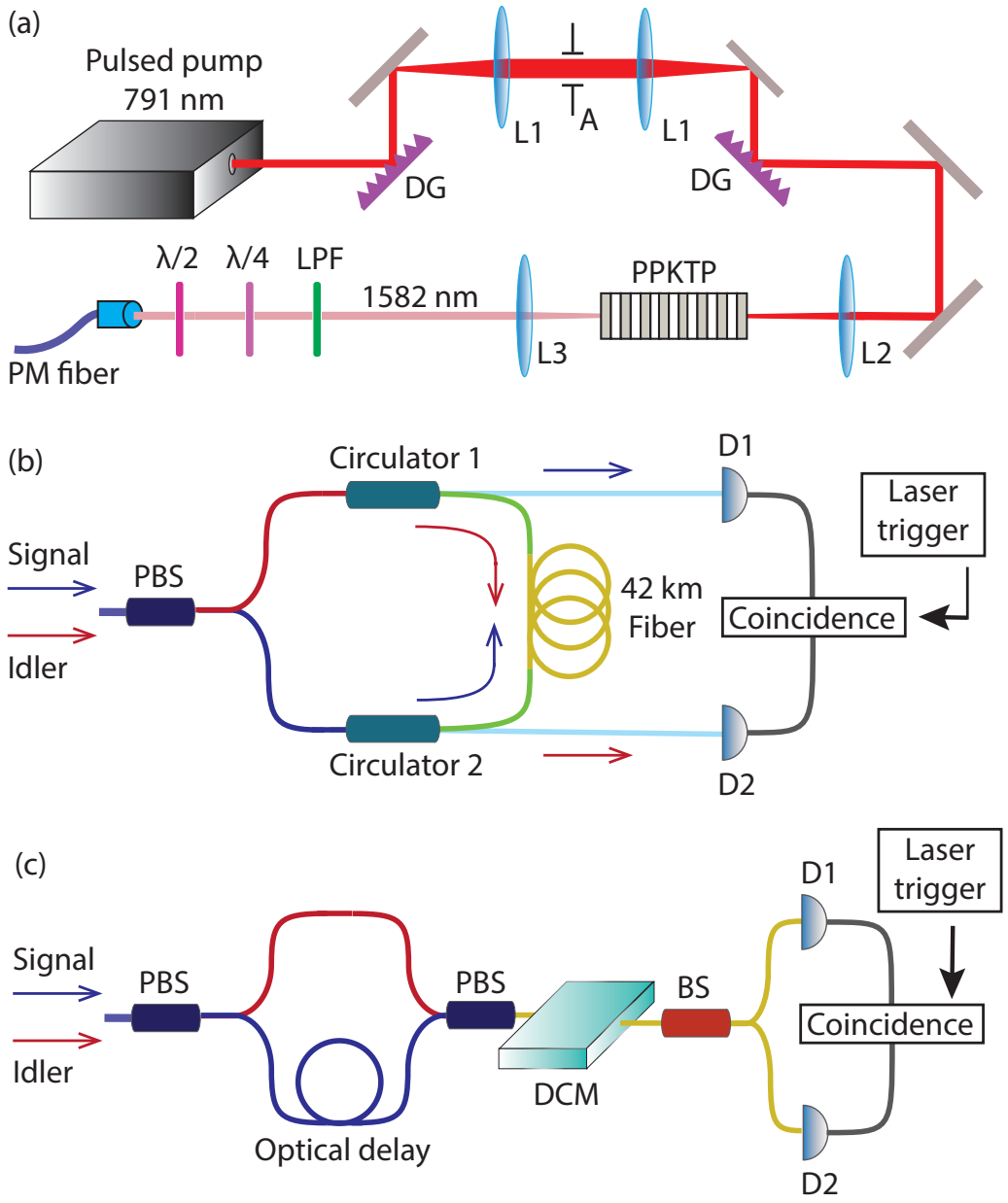

Figure 4-1: Schematics of experiment setups. (a) SPDC photon pairs generation and collection. Pump spectrum is controlled using a pair of diffraction gratings (DGs) in a $4f$ optical configuration. (b) Single-fiber spectrometer with counter-propagating signal and idler and coincidence detection by SNSPDs D1 and D2. (c) DCM spectrometer providing high resolution JSD measurements. A, rectangular aperture; L1, $f = 20\,\text{cm}$ lens; L2, $f = 40\,\text{cm}$ lens; L3, $f = 10\,\text{cm}$ lens; LPF, long-pass filter; PBS, polarization beam splitter.

the fiber, we achieved the initial alignment from the pump to the SPDC collection fiber. The pinhole was left in place for the aligned system so that any beam path drifts could be monitored.

The next step would be putting the crystal at the minimum pump beam waist location. We connected the collection fiber to a fiber-based polarization beam splitter whose outputs were connected to two WSi SNSPDs. Photon-pair arrivals would be detected if the crystal was positioned correctly relative to the pump beam. However, the crystal angle relative to the input pump beam was critical. If the incident angle of the pump was not normal to the crystal, the effective poling period would not be 46.1 μm, which might result in a lower temperature for wavelength-degenerate operation. Therefore, a fine adjustment of the crystal orientation was important to obtain a degenerate temperature near room temperature. This orientation could be roughly estimated by finding the orientation that generated the maximum number of photon pairs.

4.1.3 Chirped pump Characterization

The spectral filter system can either perform like a pulse stretcher or pulse compressor depending on the orientations and the positions of the two diffraction gratings. For our purpose of generating pure-state heralded single photons, we require a transform-limited pump at 0.95 nm bandwidth. In this section, we quantify the amount of dispersion introduced by the spectral filter system and show that the pump is transform-limited at 0.95 nm bandwidth.

In our experiement, the positions of the diffraction gratings were adjusted to minimize the broadening of the pump temporal duration after the gratings. The pulse duration was measured using an APE pulseCheck autocorrelator. When the input pump spectrum had a FWHM of 6.25 nm, we measured the pump duration before and after the spectral filter system to be 141 fs and 166 fs, which corresponded to a pulse broadening ratio of 1.2. The autocorrelation measurements are shown in Fig. 4-2. Based on the autocorrelation measurements, we found that our spectral filter system introduced a dispersion of 4289 fs^2. At 0.95 nm pump bandwidth, this small amount of dispersion can be neglected and the pump is essentially transform-limited. This was verified by comparing the Fourier transform of the measured spectrum of the

Figure 4-2: 6.25-nm pump autocorrelation measurements before and after the spectral filter system. The left figure shows the pump pulse duration before the spectral filter system and the right figure shows the pump pulse duration after the spectral filter system. A factor of $1/\sqrt{2}$ exists between the real pulse width and the measured quantity.

0.95-nm pump and its measured pulse duration. The calculated pulse duration from the measured spectrum was 2.13 ps. The convolution process in the autocorrelation measurement was taken into account in this calculation. The measured pulse duration is 2.07 $\pm$ 0.07 ps. We see that the two numbers are in good agreement.

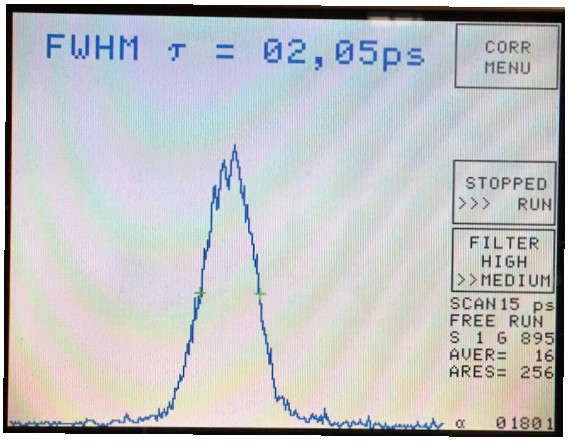

Figure 4-3: Autocorrelation measurement of 0.95-nm pump. The average measurement results of 3 measurements is 2.07 $\pm$ 0.07 ps.

We notice that some amount of higher order dispersion is introduced by the $4f$ system. This is evident from the non-Gaussian pulse shape measured after the spectral filter system. However, this only shows up when the pump bandwidth is large. In the case of 0.95-nm pump, the introduced higher order dispersion can be neglected.

An autocorrelation measured result at 0.95-nm pump is shown in Fig. 4-3.

4.2 Fiber-based JSD measurements

4.2.1 Experiment Setup

Fig. 4-1(b) shows the single-fiber spectrometer setup for characterizing the joint spectral density of the SPDC output from our custom-fabricated PPKTP. We first separated the fiber-coupled signal and idler with a fiber polarization beam splitter and sent them through a 42-km SMF28 fiber from its opposite ends. Two fiber circulators were used to provide input/output isolation for both signal and idler light before detection by two SNSPDs with detection efficiencies of ∼80%, timing jitter of ∼200 ps, and dark count rates of ∼400/s. The dark count rates were low enough that no background subtraction adjustment was needed for all measurements. The use of a single fiber ensures that the counter-propagating signal and idler see the same amount of dispersion. The fiber was thermally shielded to reduce variations in length and dispersion due to ambient temperature fluctuations during measurements. The arrival times of signal and idler photons were recorded relative to the trigger pulses from the mode-locked pump laser. Due to fiber dispersion the propagation times of different spectral components propagate at different speeds resulting in different arrival times, therefore allowing the JSD to be reconstructed based on the measured coincidence timing information.

4.2.2 Experiment Results

The spectral resolution of our 42-km fiber spectrometer is set by the dispersion imposed by the fiber and the temporal measurement resolution given by the SNSPDs' timing jitter of 200 ps. The dispersion of the 42-km fiber was measured to be 0.78 ± 0.07 ns/nm at 1582 nm, in line with manufacturer's published data. Therefore our single-fiber spectrometer had a spectral resolution of ∼0.25 nm for both signal and idler. The spectrometer's insertion loss was ∼10 dB per channel that was primarily due to the fiber, suggesting a reduction of 100 fold in the coincidence detection rate when compared to measurements without the spectrometer. Fig. 4-4 shows the mea-

sured log-scale JSD distribution at six different pump bandwidths without the use of any spectral filtering. The wavelength range was 16 nm centered at 1582 nm that was set by the pump's mode-locking repetition period of 12.5 ns and the fiber's dispersion of 0.78 ns/nm. The peaks of the JSD distributions for all cases are set to center at 1582 nm that corresponds to the signal and idler degenerate wavelength, thereby setting the correct timing delay we applied relative to the trigger pulses. We then used the dispersion we had measured (0.78 ns/nm) to map the detected arrival times to the corresponding wavelengths. We only use a linear relation between frequency and time of arrival because any nonlinear adjustment is not significant compared with the relatively large detector timing jitter.

It is known that PPKTP under extended phase-matching and pulsed pumping generates coincident-frequency entangled photon pairs [18, 27, 28, 39]. That is, signal and idler have the same frequencies and their JSD profile is diagonal, as shown in Fig. 4-4. We see that the wavelength extent of the signal and idler outputs (along the diagonal) is reduced as the pump bandwidth varies from 5.6 nm to 0.74 nm, as expected. The pump spectrum remained approximately Gaussian for the different measurements and the pump bandwidths reported are Gaussian fitted measurements. Overall, the JSD measurements match our theoretical expectations very well. Two particular features of Fig. 4-4 are worth mentioning. The first is that the strongest side lobe of the profiles is at least 24 dB below the central peak, which corresponds to an 11 dB suppression of the side lobes of the standard phase-matching sinc function. This is a more sensitive and therefore more accurate measurement of the residual side lobes than the DFG measurements of Fig. 3-3, suggesting that the Gaussian profile of our custom fabrication design is quite good. The second feature is the nearly circularly symmetric profile of the central lobe in Fig. 4-4(e) that is consistent with a factorable biphoton output at the pump bandwidth of 0.95 nm.

To quantify the spectral correlation of the generated biphoton states in Fig. 4-4, we assume that the biphoton state is transform limited so that we can perform a singular value decomposition for continuous variables on the square root of our measurement results to obtain the Schmidt number. The heralded-state purity is given by the inverse of the Schmidt number. The Schmidt number and the corresponding purity at different pump bandwidths are listed in Table 1:

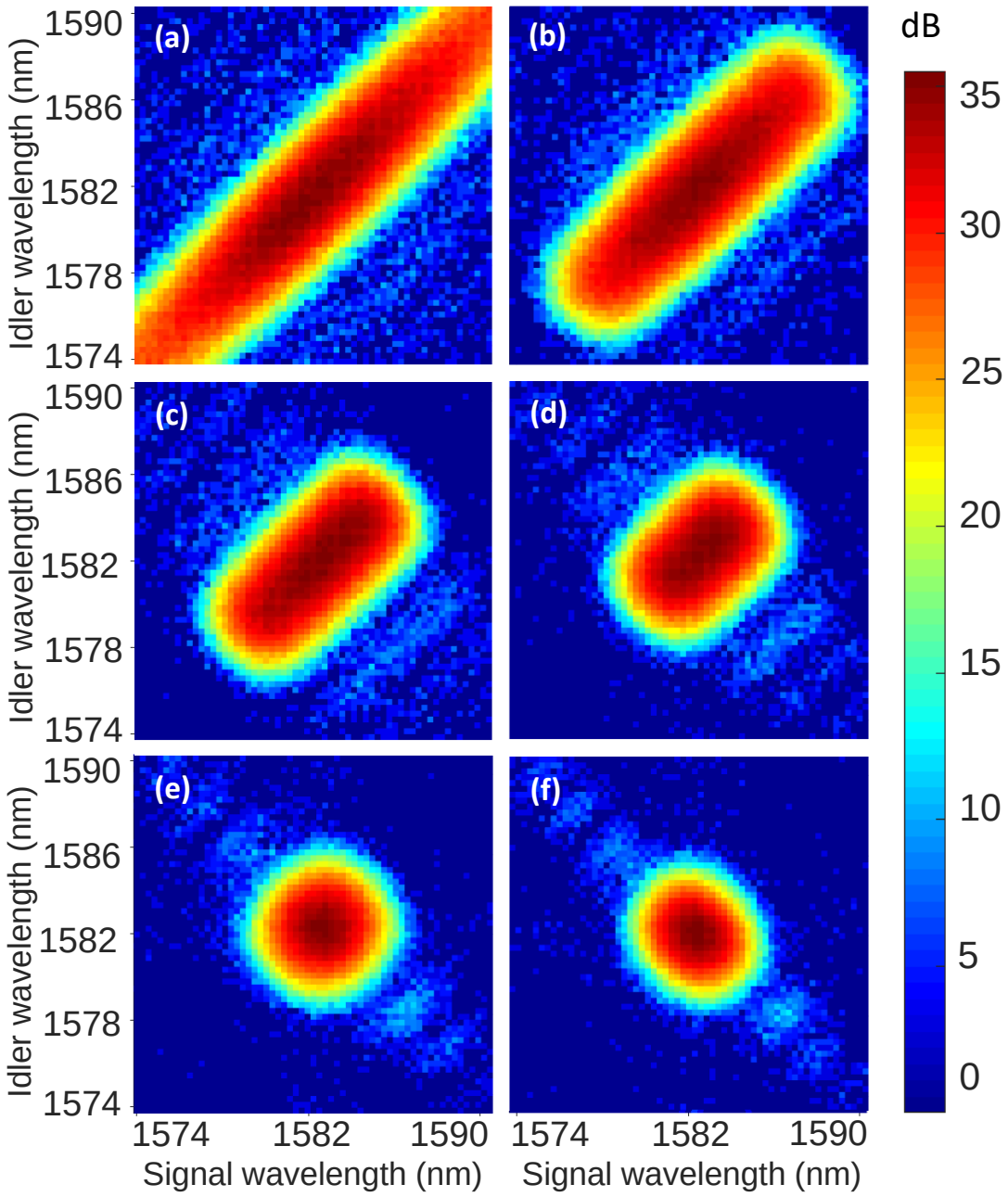

Figure 4-4: JSD measurements from single-fiber spectrometer in log scale. From (a) to (f), the pump bandwidths are 5.6 nm, 3.6 nm, 2.4 nm, 1.6 nm, 0.95 nm, and 0.74 nm, respectively.

Table 4.1: Inferred heralded-state spectral purity of Fig. 4-4 measurements

Pump bandwidth (nm)	Schmidt number	Purity
5.6	2.56	39%
3.6	1.92	52%
2.4	1.41	71%
1.6	1.13	88%
0.95	1.01	99%
0.74	1.03	97%

As expected, the purity improves as the JSD profile goes from highly elliptical for broad pump bandwidths to the circularly symmetric case for a pump bandwidth of 0.95 nm, at which a biphoton state of 1.01 Schmidt number with a corresponding heralded-state purity of 99% is achieved. A biphoton state yielding high heralded-state purity such as that shown in Fig. 4-4(e) indicates very little frequency correlation between signal and idler, and that such a biphoton state can be ideally suited for generating heralded pure-state single photons. Note that the purity calculation is based on the assumption that the joint distribution of signal and idler amplitudes are transform limited in frequency and time. Therefore, our calculated purity can only serve as an upper limit at this point. To verify this assumption, additional measurements of the biphoton state in the time domain, or Hong-Ou-Mandel interferometric measurements between photons from independent sources [50, 51] are needed. However, previous measurements have suggested that the biphoton state generated from SPDC is transform limited based on indirect evidence [18].

4.2.3 Fiber Dispersion Calibration

The resolution of our JSD is entirely determined by the amount of dispersion, given a fixed detector timing jitter. Therefore, measuring the amount of dispersion introduced by the 42-km of fiber is important.

The key to measuring the fiber dispersion is to utilize a reference marker. For standard SMF28 fibers, 1310 nm is the zero-dispersion wavelength and can be used as a reference. To perform the measurement, we first combined a tunable cw beam set at the desired wavelength and a 1310-nm cw beam. Both beams were then sent to an intensity modulator which produced 1-ns sharp pulses at 10 MHz repetition rate. Both pulses were then sent through the 42-km fiber. A fast detector with sufficient

bandwidth was used to detect the pulses. By scanning through the desired wavelength range and monitoring the arrival time difference between the desired-wavelength beam and the 1310-nm beam using an oscilloscope, we were able to measure the total time delay due to dispersion. The relative delay per nm was then calculated to be 0.77 $\pm$ 0.11 ns/nm.

There was another reference that could be used besides the 1310-nm beam. We used the electrical trigger that drove the intensity modulator for pulse generation as our reference and the measured relative time delay per nm was 0.78 $\pm$ 0.09 ns/nm. There is no reason for preferring one reference to the other since they give the same measurement results.

4.2.4 Pump, Signal, and Idler Bandwidths

There is a relationship between the pump bandwidth and the generated signal or idler bandwidth when the JSD is circularly symmetric. Under extended phase matching, the pump frequency is along the anti-diagonal $\omega_s + \omega_i =$ constant axis in JSD plot. If we perform a coordinate transformation, we can see that the diagonal axis unit vector is $\sqrt{2}$ times the ω_s or ω_i axis unit vector. Therefore, the pump bandwidth is equal to $\sqrt{2}$ times the signal and idler bandwidth in frequency.

Alternatively, we can try to understand this relation from an energy perspective. Let us assume the signal and idler are independent of each other, the total variance of signal and idler spectral distribution will be the sum of the individual variance. Because the energy is always conserved, the variance sum of signal and idler spectral distribution is equal to the variance of the pump spectral distribution. Therefore, the bandwidth of the pump is $\sqrt{2}$ times larger than the bandwidth of signal or idler. This relation can be used for checking whether the JSD measurement results obtained are reasonable.

4.3 JSD Measurements using Dispersion Compensation Module

To measure the JSD profile more efficiently and with higher resolution, we implemented a different spectrometer based on a commerically available dispersion compensation module (DCM) instead of a long optical fiber. The DCM uses reflective chirped fiber Bragg gratings to compensate fiber dispersion in long-distance fiber-optic transmission with low insertion loss and low latency. Most relevant to our application is that it has a fixed insertion loss regardless of the amount of its dispersion. Our DCM from Proximion is specified to have a dispersion of 1.88 ns/nm at 1585 nm and an insertion loss of 2.8 dB. For comparison, 100 km of fiber gives the same amount of dispersion but incurs an insertion loss that is 50× higher. Furthermore, the DCM is insensitive to ambient temperature fluctuations and hence thermal stabilization is unnecessary.

4.3.1 Experiment Setup

We chose to use a single DCM for the spectrometer and intended to send the orthogonally polarized signal and idler through the DCM before separating them with a fiber PBS for subsequent detection. Unfortunately, the DCM had a wavelength dependent polarization mode dispersion of ∼0.6 ps such that the output signal and idler polarizations would be elliptical and no longer orthogonal. In other words, signal and idler cannot be separated based on their polarizations after passing through the DCM. To work around this technical issue, we applied a fixed time delay between signal and idler as identification tags, as shown in the DCM spectrometer configuration of Fig. 4-1(c). After separating signal and idler with a fiber PBS, we added an optical delay of 11.7 ns to the signal path before recombining them with a second fiber PBS and sending them through the DCM. We sent the combined outputs through a 50:50 fiber beam splitter so that about half of the time the signal and idler would be separated and detected by the two WSi SNSPDs. The time separation between signal and idler is much less than the SNSPD recovery time of ∼80 ns and their detection on the same side of the beam splitter output would not be possible. The time-delay scheme incurs

effectively a 3 dB insertion loss but allows us to use a single-DCM implementation. In principle, we could use two DCMs to avoid the 3 dB penalty, one for signal and the other for idler, as long as the DCMs have identical dispersion or if they are well calibrated [52, 53].

4.3.2 Experiment Results

Figure 4-5 shows the JSD profile and the marginal distributions for the biphoton state for a pump bandwidth of 0.95 nm using the DCM spectrometer, with a spectral resolution of 0.11 nm that is more than two times better than that of the single-fiber spectrometer. Because the coincidence measurement interval was limited by the pump repetition period of 12.5 ns, the wavelength range of Fig. 4-5 is limited to ∼6.6 nm. The higher resolution measurement of the JSD distrbution of Fig. 4-5(a) clearly displays a highly symmetric profile, much like the lower resolution profile of Fig. 4-4(e). We note that because the wavelength range is limited to 6.6 nm, the residual side lobes that are visible in Fig. 4-4(e) are mostly out of range. Based on this higher-resolution profile, we obtain a purity estimate of 99.3% that is slightly higher than that measured with the single-fiber spectrometer of Fig. 4-4(e). The slightly higher value is due to the exclusion of the residual side lobes in the smaller wavelength range of the DCM spectrometer, suggesting that the degradation due to the highly suppressed side lobes is very small. The high purity we have achieved without the use of any spectral filtering is entirely the result of the Gaussian phase-matching function of our custom PPKTP cyrstal. We confirm that the marginal distributions shown in Fig. 4-5(b) are Gaussian as a result of the custom phase-matching function.

It is useful to recognize the role played by the Gaussian phase-matching function by comparing our results with previous JSD measurements based on PPKTP cyrstals with the standard sinc-function phase matching. Table 2 shows the comparison. Without applying spectral filtering none of these measurements with the standard sinc-shaped phase matching achieved purity higher than 93%. Weston *et al.* obtained an inferred purity close to 100% using an 8-nm filter applied to the SPDC outputs with a FWHM bandwidth of 15 nm [26]. That is, near-unity purity has only been achieved by strong spectral filtering unless the standard phase matching is modified to assume a Gaussian shape as done in our work [31].

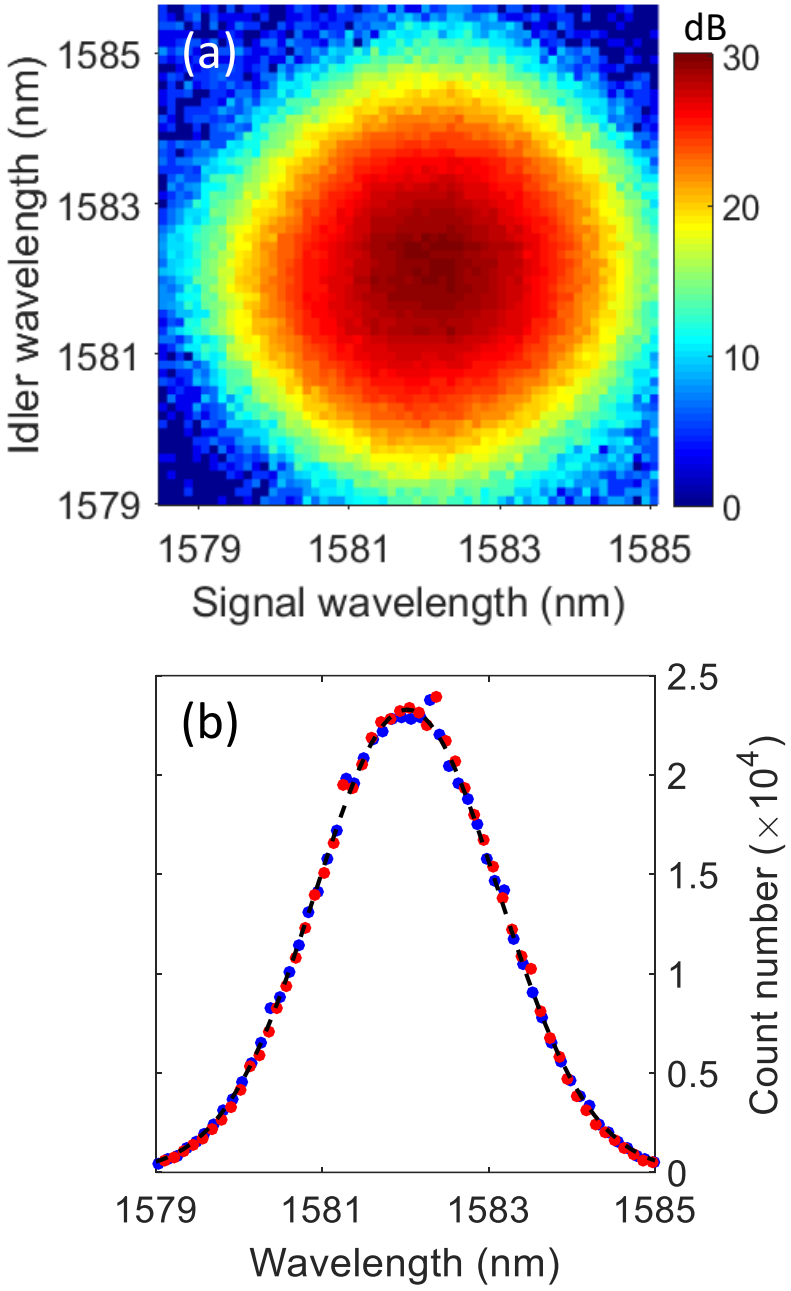

Figure 4-5: JSD and marginal distributions of biphoton state for 0.95 nm pump bandwidth. (a) High-resolution JSD measurements with 0.11 nm resolution in log scale. (b) Signal (idler) marginal distribution is shown in blue (red) in linear scale per 0.11-nm bandwidth. Dashed line is Gaussian for comparison.

Table 4.2: Comparison of spectral purity measurements

References	Spectral filter	Purity
Kuzucu *et al.* [18]	None	88%
Gerrits *et al.* [19, 24]	None	93%
Yabuno *et al.* [21]	None	83%
Jin *et al.* [22]	None	82%
Harder *et al.* [23]	8 nm	84%
Kaneda *et al.* [25]	None	91%
Weston *et al.* [26]	8 nm	∼100%
This thesis	None	99%

4.3.3 Hydraharp Time Tagging

For all experiments, we used the hydraharp from PicoQuant to time tag all events. In this section, we digress from the main topic and briefly discuss the time tagging method using the hydraharp.

Hydraharp offers three different time tag modes. There are the histogram mode, ht2 mode, and ht3 mode. The histogram mode produces a histogram of event arrival times of the input channel relative to the sync channel. An event is registered in the histogram when there is a sync signal and an input signal received. And the arrival time is the time difference between the input and sync signal (input signal should arrival later than sync signal). The timing resolution and a constant timing offset can be set in the hydraharp. The integration time of each measurement can also be adjusted. For coincidence measurements, we used a 2-ns timing resolution, which corresponded to a 2 ns coincidence window; and a 45-ns input signal delay, which centered the coincidence peak at 45 ns instead of 0 ns relative to the sync signal. Unfortunately, the histogram mode does not work for more than one input channel. It is worthwhile to note that the hydraharp also calculates a sync and input channel count rates and displays them as channel count rates. The displayed channel count rates are not the true counts received each second and are not trustworthy.

The ht2 mode records all event arrival times for all connected channels from start to finish at 1 ps resolution. Therefore, no sync input is required in the ht2 mode. Furthermore, a sync input in this mode will be no different from a regular input. Although the timing resolution cannot be changed, a constant timing offset can still be added to each individual inputs. The ht2 mode outputs a binary file that contains

all the events' arrival times. However, it is not directly accessible. It has to be converted into a .txt file for viewing and reading purposes. The suggested program used for conversion is C or C++. Conversion using MATLAB is very slow and may result in many errors. After the raw file is converted to a readable format. It can be further analyzed by one's program of choice.

The ht3 mode records all events' arrival times for all input channels relative to the sync signals. The resolution and timing offset of each channel are both adjustable in this mode. Similar to ht2, it outputs a binary file that needs additional processing in order to view or read the recorded data. Unlike the ht2 mode, in which all event arrival times are recorded, ht3 mode records the number of sync it received sequentially and the input arrival times with respect to the latest received sync signal. Therefore, for all cases, a periodic sync signal is desired in order to know the absolute arrival time information of the input signals. Unfortunately, all hydraharp channels cannot receive a high flux input more than 12.5 MHz. For a sync channel that has a repetition rate higher than 12.5 MHz, we need to use the divider option to match the actual input sync rate and the internal logic sync rate of the hydraharp. If the sync rate is random or lower than 1 MHz, the divider option should be turned off.

Chapter 5

Photon Pairs Indistinguishablility and Spectral Entanglement

5.1 Photon Pairs Indistinguishablility

Extended phase matching is a technique that generates coincident-frequency entanglement such that it restores signal and idler indistinguishability in pulsed SPDC that can be confirmed with Hong-Ou-Mandel interference measurements. In this section, we examine the indistinguishability between the signal and idler photons.

5.1.1 Hong-Ou-Mandel Interference

Hong-Ou-Mandel interference [54] is a quantum phenomenon that can be used for measuring photon bandwidth, biphoton coherence time, and input photons' indistinguishability. This phenomenon occurs when two photons interfere at a 50:50 beam splitter. If the two input photons are indistinguishable in all their properties including spatial, spectral, and temporal modes, they always exit together at one of the two output ports.

Generally, when two photons enter a 50:50 beam splitter, there are four different possible ways for them to exit the beam splitter. Both photons can exit from different ports, meaning they both get transmitted or reflected. Or both photons can exit from the same port of the beam splitter. In the case they exit the same port, one photon gets transmitted while the other one gets reflected. Here, we analyze this phenomenon

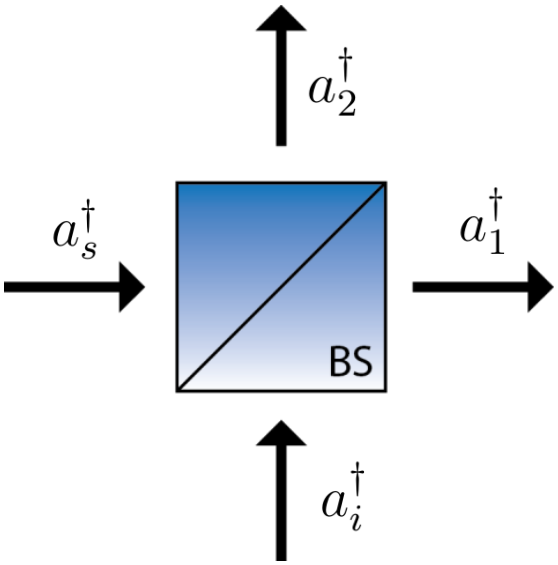

Figure 5-1: The inputs to a beam splitter with transmissivity η are $\hat{a}_s^\dagger$ and $\hat{a}_i^\dagger$. The outputs from the beam splitter are $\hat{a}_1^\dagger$ and $\hat{a}_2^\dagger$.

from a quantum mechanical point of view.

Consider a lossless beam splitter with power transmissivity η and reflectivity $1-\eta$ with two photons with single-mode creation operators, $\hat{a}_s^\dagger$ and $\hat{a}_i^\dagger$. The outputs from the beam splitter are $\hat{a}_1^\dagger$ and $\hat{a}_2^\dagger$, as illustrated in Figure 5-1. We can write the beam splitter input-output relations as:

$$\hat{a}_1^\dagger = \sqrt{\eta}\ \hat{a}_s^\dagger + \sqrt{1-\eta}\ \hat{a}_i^\dagger, \tag{5.1}$$

$$\hat{a}_2^\dagger = -\sqrt{1-\eta}\ \hat{a}_s^\dagger + \sqrt{\eta}\ \hat{a}_i^\dagger. \tag{5.2}$$

Because we assume the beam splitter is lossless, and the energy is conserved, the input and output operators obey:

$$\hat{a}_1^\dagger \hat{a}_1 + \hat{a}_2^\dagger \hat{a}_2 = \hat{a}_s^\dagger \hat{a}_s + \hat{a}_i^\dagger \hat{a}_i. \tag{5.3}$$

Using Eqs. (5.1) and (5.2), we can write the beam splitter's input-output relation in matrix form:

$$\begin{bmatrix} a_1^\dagger \\ \hat{a}_2^\dagger \end{bmatrix} = \begin{bmatrix} \sqrt{\eta} & \sqrt{1-\eta} \\ -\sqrt{1-\eta} & \sqrt{\eta} \end{bmatrix} \begin{bmatrix} a_s^\dagger \\ \hat{a}_i^\dagger \end{bmatrix} \tag{5.4}$$

Because we know the input state is:

$$|\psi\rangle_{in} = a_s^\dagger a_i^\dagger |00\rangle = |11\rangle . \tag{5.5}$$

Therefore, we can calculate the output state to be:

$$|\psi\rangle_{out} = \begin{bmatrix} \sqrt{\eta} & \sqrt{1-\eta} \\ -\sqrt{1-\eta} & \sqrt{\eta} \end{bmatrix} |\psi\rangle_{in} \tag{5.6}$$

$$= (\sqrt{\eta}\ \hat{a}_s^\dagger + \sqrt{1-\eta}\ \hat{a}_i^\dagger)(-\sqrt{1-\eta}\ \hat{a}_s^\dagger + \sqrt{\eta}\ \hat{a}_i^\dagger)\,|00\rangle \tag{5.7}$$

$$= \left[(2\eta-1)\hat{a}_s^\dagger\hat{a}_i^\dagger + \sqrt{\eta(1-\eta)}(\hat{a}_i^\dagger\hat{a}_i^\dagger - \hat{a}_s^\dagger\hat{a}_s^\dagger)\right]|00\rangle \tag{5.8}$$

$$= (2\eta-1)\,|11\rangle + \sqrt{2\eta(1-\eta)}(|02\rangle - |20\rangle), \tag{5.9}$$

where the terms $|02\rangle$ and $|20\rangle$ correspond to the cases in which both photons exit together. The $|11\rangle$ term corresponds to the case in which photons exit from different ports, resulting in a coincidence count. If the beam splitter has a 50:50 splitting ratio ($\eta = \frac{1}{2}$), the coincidence term $(2\eta-1)\,|11\rangle$ in Eq. (5.9) becomes zero. The leftover term is $\sqrt{2\eta(1-\eta)}(|02\rangle - |20\rangle)$. The beam splitter output state then becomes:

$$|\psi\rangle_{out} = \frac{1}{\sqrt{2}}(|20\rangle - |02\rangle). \tag{5.10}$$

The state is normalized because $(\hat{a}^\dagger)^n\,|0\rangle = \sqrt{n!}\,|n\rangle$. We notice that the output in Eq. (5.10) state only has $|02\rangle$ or $|20\rangle$ state, therefore, the photons always exit together and there is no coincidence event. If the beam splitter does not have a 50:50 splitting ratio, there are chances where two photons exit from different ports of the beam splitter. If the beam splitter transmissivity is η, then the cross term in Eq. (5.9) is $(2\eta-1)\,|11\rangle$. The probability of occurrence is thus $(2\eta-1)^2$.

In a typical HOM interference measurement where the goal is to measure the two inputs' indistinguishability, the two inputs are first sent in with a constant relative time delay. Because of the timing difference, the two photons are distinguishable. Two single photon detectors are placed at each output of the beam splitter. If each of the two detectors detects a photons at the same time, we know the photons exit from different ports. If only one detector gets a detection, either they exit from the

same port or one of the photons does not get detected. In either case, it is considered that there is no coincidence. By performing this coincidence counting, we can tell how often they exit from different ports. As the relative time delay decreases, the two inputs become more and more indistinguishable. A drop in coincidence is then observed.

To quantify the photons indistinguishability, we define the HOM interference visibility as:

$$V = \frac{N_{\max} - N_{\min}}{N_{\max} + N_{\min}} \tag{5.11}$$

where $N_{\max}$ is the maximum coincidence observed when the two identical photons are not overlapped in time, and $N_{\min}$ is the minimum coincidence observed when the two photons are overlapped in time. The visibility will have a value of 1 if the two photons are indistinguishable and a value of 0 if the two photons are completely distinguishable.

We can then estimate the decrease in visibility caused by an imperfect 50:50 beam splitter, given the two inputs are perfectly identical. If there are 1000 singles at each input port, then the maximum coincidence count will be 500. Assuming we have 49:51 beam splitter, the resulting coincidence probability will be $(2 \times 0.49 - 1)^2 = 0.0004$, which is about 0.4 counts. Using the definition in Eq. (5.11), we see the maximum visibility achievable is 99.8%.

5.1.2 HOM Interference Measurement Setup

We made the HOM interference measurements with SPDC signal and idler as inputs for a pump bandwidth of 5.6 nm. To minimize multi-pair emission, the applied pump power was set to 0.25 nJ per pulse and the mean generated photon pair per pulse was ∼0.3%. After the signal and idler were separated by a fiber PBS, they were sent to interfere at a 50:50 fiber beam splitter with an adjustable air gap delay for one of the input arms. The coincidence counts were detected by two SNSPDs. A setup schematic is shown in Fig. 5-2.

The relative time delay between signal and idler is crucial for this experiment. When the relative time delay is large, there should be no drop in coincidence counts. We used a superluminescent diode (SLD) at 1550 nm to find the zero path length

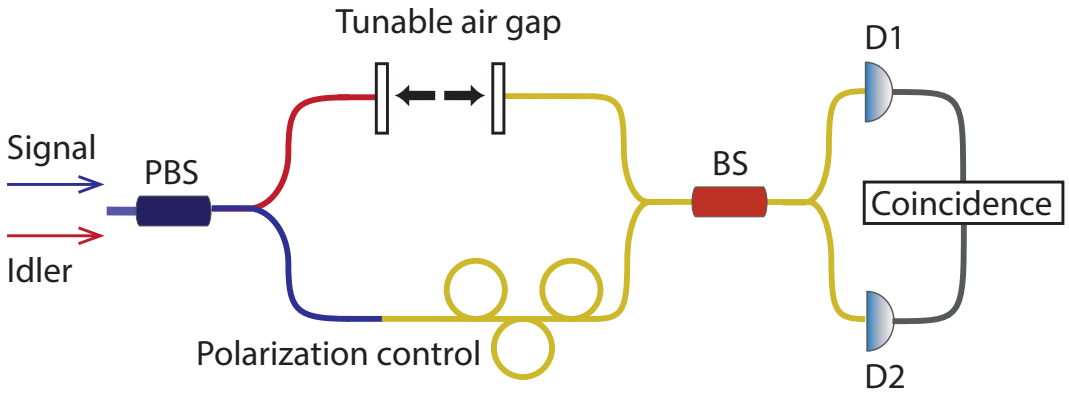

Figure 5-2: Schematic of Hong-Ou-Mandel interference measurement setup. PBS, polarization beam splitter; BS, beam splitter; D1, SNSPD 1; D2, SNSPD 2.

difference location, which is also the zero time delay location. We used the SLD as the input to the PBS and monitored one output of the BS with an InGaAs detector. Because the SLD has a large bandwidth (over 50 nm) and a short coherence length, interference of SLD would only be observed if the path lengths were equal. Therefore, the path length difference of signal and idler can be determined within an accuracy of 15 μm without measuring the fiber length.

Once the equal-path-length location is found, the idler's polarization is changed to match the signal's polarization. The crystal temperature was then maintained at the degenerate temperature to ensure a frequency degenerate signal and idler. If the polarization and the crystal temperature are set correctly, the coincidence should be close to zero at the equal-path-length location.

5.1.3 HOM Interference Measurement Results

For standard type-II phase matching, the sinc-shaped function leads to an inverted triangular interference dip in HOM interference. For Gaussian-shaped phase matching, it is expected that the HOM interference should exhibit a Gaussian shape instead [25]. The detected coincidence counts per second versus the air gap delay without and with a 10-nm bandpass filter centered at 1582 nm for a pump bandwidth of 5.6 nm are shown in Fig. 5-3 and Fig. 5-4.

As expected, the measured data follow the Gaussian shape shown as the dashed

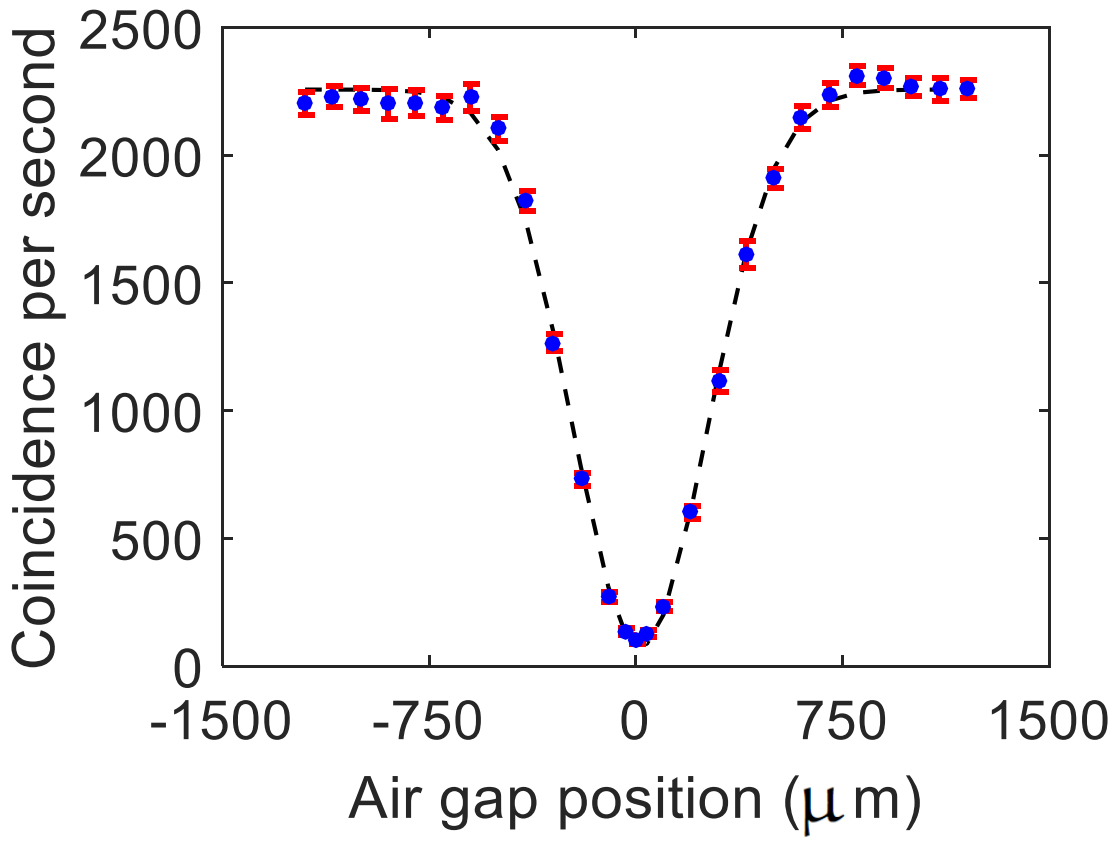

Figure 5-3: HOM interferometric measurements without filtering. The Gaussian shape dip has a visibility of 92%. Markers are data points with error bars of one standard deviation and dashed curves are Gaussian fits. The pump bandwidth is 5.6 nm and no background subtraction is applied.

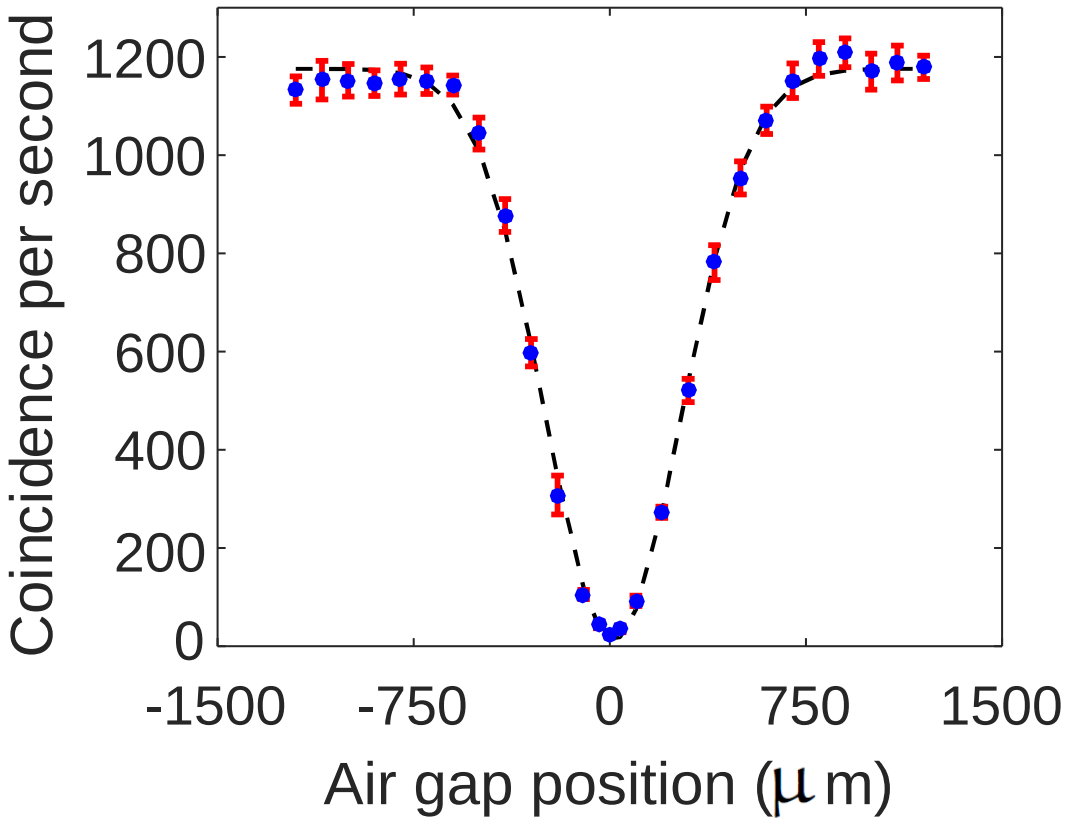

Figure 5-4: HOM interferometric measurements with a 10-nm bandpass filter. The Gaussian shape dip has a visibility of 96%. Markers are data points with error bars of one standard deviation and dashed curves are Gaussian fits. The pump bandwidth is 5.6 nm and no background subtraction is applied.

curve in Fig. 5-3. The HOM interference visibility is found to be 92% (without background subtraction). The high visibility implies a high degree of indistinguishability between signal and idler, but it does not reach its asymptotic value of unity visibility that is expected under ideal extended phase-matching conditions [28]. By applying a mild filter of 10 nm bandwidth, the HOM interferometric measurement of Fig. 5-4 shows an improved visibility of 96%, suggesting that removing the residual side lobes are useful in improving the signal-idler indistinguishability. The measured visibility of 96% is actually quite close to the expected value of 97.8%, given that we estimate a visibility degradation of 2.2% owing to imperfect PBS (1% leakage of the wrong polarization) and a fiber beam splitter with a splitting ratio of 49:51. Additional degradation could be caused by polarization drifts during measurements. A Gaussian fit of our measured data, as shown in Fig. 5-3, gives a visibility of $94 \pm 2\%$ without filter, and a visibility of $98 \pm 2\%$ with the filter. The stated uncertainty corresponds to the 95% confidence fitting bounds.

From the HOM interferometric measurement of Fig. 5-3 we obtain a biphoton coherence time (FWHM) of 1.92 ± 0.06 ps, which yields a biphoton coherence bandwidth (FWHM) of 1.92 ± 0.06 nm for a Gaussian time-frequency transform limited pair with a time-bandwidth product $\Delta f \Delta\tau = 2\ln 2/\pi \approx 0.44$, where Δf ($\Delta\tau$) is the full-width at half-maximum of frequency bandwidth (time duration). Under extended phase matching, this biphoton coherence bandwidth should also equal the SPDC phase-matching bandwidth that we can obtain from the DFG measurements in Fig. 3-2 to be 2.2 ± 0.4 nm. The two values are in reasonable agreement and that the difference is possibly due to deviation from ideal extended phase-matching conditions and the relatively large measurement uncertainty of the DFG measurement. In the ideal case [28], the biphoton coherence bandwidth is only a function of the signal-idler frequency difference and hence the phase-matching function, and does not depend on the pump bandwidth. Indeed, one observes in Fig. 4-4 that the widths of the JSD distributions along the anti-diagonal axis are more or less the same for pump bandwidths ranging from 5.6 nm to 0.74 nm.

Furthermore, the HOM interference does not change at different pump bandwidths as we have discussed in Chapter 2. The HOM interferometric measurement results at various bandwidths are shown in Fig. 5-5. It is also worthwhile to briefly discuss

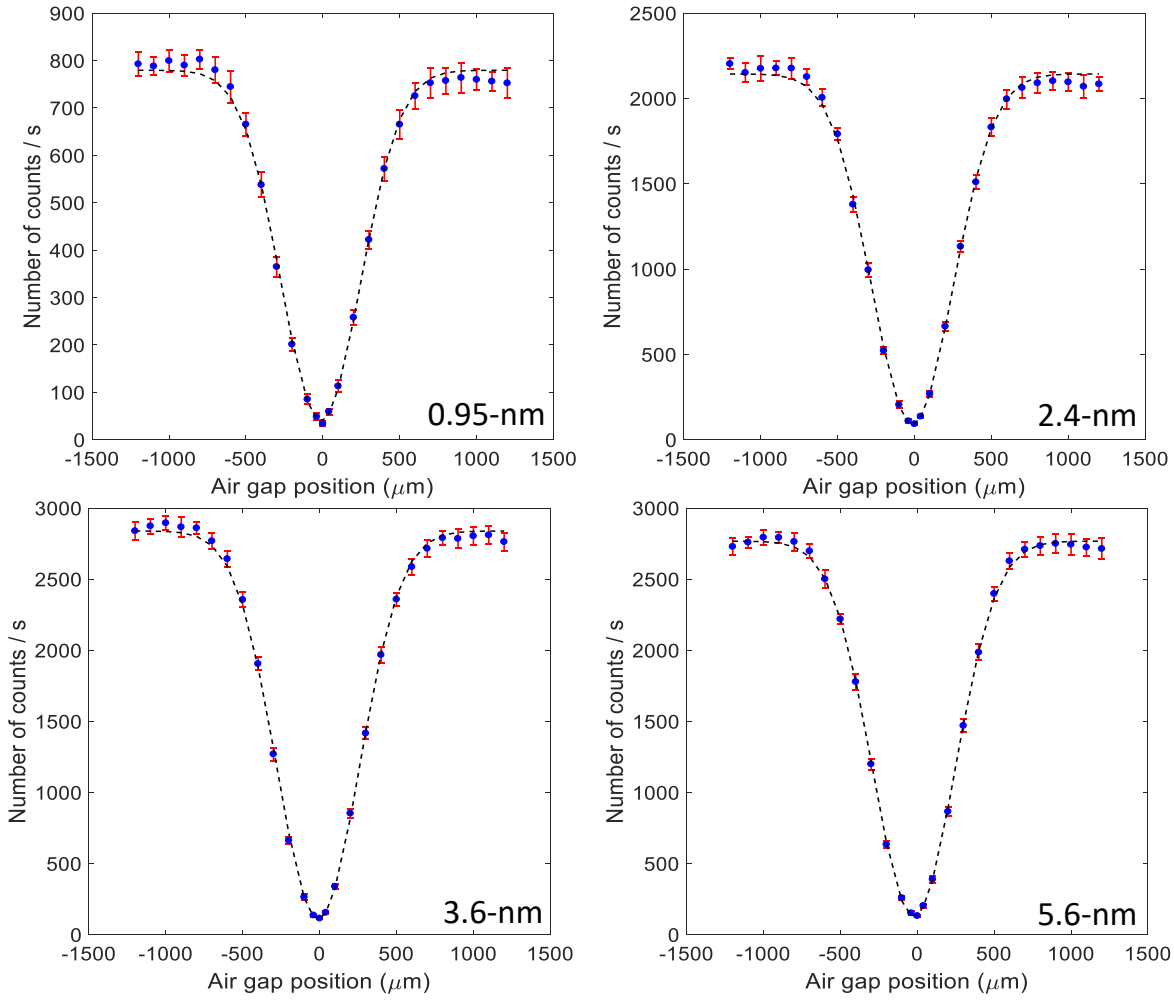

Figure 5-5: HOM interferometric measurements at various pump bandwidths. Markers are data points with error bars of one standard deviation and dashed curves are Gaussian fits. The interference visibilities obtained from Gaussian fitted results are: 92.0% at 0.95-nm pump; 91.9% at 2.4-nm pump; 92.6% at 3.6-nm pump; 91.2% at 5.6-nm pump.

the effect of dispersion on the HOM dip bandwidth. We examined the change of HOM dip width due to dispersion when signal and idler pairs were both sent through a long fiber with large amount of dispersion ($\sim 200\,\mathrm{m}$ standard SMF28 fiber). We observed that the HOM dip bandwidth did not change. The biphoton coherence time is insensitive to dispersion experienced by both signal and idler. For anti-correlated SPDC photon pairs, their resultant HOM dip width is unchanged even if one goes through a dispersive medium while the other one does not [55].

5.2 Spectral Entanglement

5.2.1 Spectrally Entangled Photon Pairs

At a pump bandwidth of 5.6 nm the JSD measurement of Fig. 4-4(a) clearly shows that the signal and idler are correlated in frequency. However, the JSD alone is insufficient for one to conclude that they are frequency entangled. Imagine a joint state that is a low-flux mixture of different types of photon pairs with the following characteristics: the photons in each pair are orthogonally polarized; the photons in each pair type have the same center frequency and the same bandwidth as the HOM interference bandwidth (which is much smaller than the JSD bandwidth); and different types of photon pairs have different center frequencies such that the combined frequency coverage spans the bandwidth given by the JSD. Such a mixed state of frequency-unentangled photon pairs would give the same JSD and HOM interference results of Fig. 4-4(a) and Fig. 5-3, respectively. To show that the pulsed SPDC output state generated under 5.6 nm pump bandwidth is frequency entangled, we made a signal (idler) field-autocorrelation measurement showing a time duration of $0.36 \pm 0.04\,\mathrm{ps}$ ($0.38 \pm 0.04\,\mathrm{ps}$) with a corresponding spectral bandwidth of 10.2 nm (9.69 nm). Our field-autocorrelation measurement uses a fiber-based Mach-Zehnder interferometer with a single-photon input of either signal or idler and yields the input's spectral bandwidth. The measured spectral widths are much larger than the phase-matching bandwidth, which proves that the joint state could not be a mixture of low-bandwidth photon pairs and confirms that the SPDC output was indeed frequency entangled [56]. We note that the marginal distributions for signal and idler from Fig. 4-4(a) yield

spectral bandwidths of 10.15 ± 0.1 nm and 10.27 ± 0.1 nm, respectively, which are in good agreement with the field-autocorrelation measurements.

To verify the SPDC spectral bandwidth at 0.95 nm pump bandwidth, we follow the same steps as those taken for confirming the spectral entanglement of the biphoton state when the SPDC was pumped with a pump bandwidth of 5.6 nm. Field-autocorrelation measurement for signal (idler) at 0.95 nm pump bandwidth yields a time duration of 1.45 ± 0.02 ps (1.41 ± 0.01 ps), which corresponds to the spectral bandwidth of 2.54 ± 0.04 nm (2.61 ± 0.02 nm). From Fig. 4-5(b) we calculate the spectral bandwidth of signal and idler to be 2.62 ± 0.04 nm and 2.60 ± 0.03 nm, respectively, which are in good agreement with the field-autocorrelation results.

5.2.2 Field-autocorrelation Measurement

We used a modified HOM interference setup to complete the field-autocorrelation measurement. The originally horizontally-polarized signal photons were rotated 45° in polarization and sent into the polarization beam splitter. Because the polarization beam splitter could only separate horizontal and vertical polarizations, it became effectively a 50:50 beam splitter for 45° polarized input. An SNSPD was used to detect the count rate of one beam splitter port as the relative path difference was scanned. The idler coherence time was measured using the same procedure with the polarization rotated idler input.

The signal photon interferes with itself if the two path lengths are equal or their difference is within the photon's coherence length. The interference incurs rapid fluctuations in single counts at the BS output because the path difference is not stabilized. To capture these rapid fluctuations, ten measurements were taken each second. Results of a signal photon autocorrelation measurement at 5.6-nm and 0.95-nm pump are shown in Fig. 5-6 and Fig. 5-7, respectively. A pump beam with broader bandwidth generates signal photon with a larger bandwidth and a shorter coherence time, which agrees with our experimental results. The idler coherence time was measured with the same procedure. The idler coherence time was found to be identical to the signal coherence time which is as expected because they are indistinguishable.

The FWHM of the signal and idler coherence time is calculated from the envelope of the count rate fluctuations. The count rate fluctuations are defined by the difference

between the maximum count rate detected and the minimum count rate detected. Background fluctuations due to dark counts or other electronic noises are subtracted from the envelope before calculation.

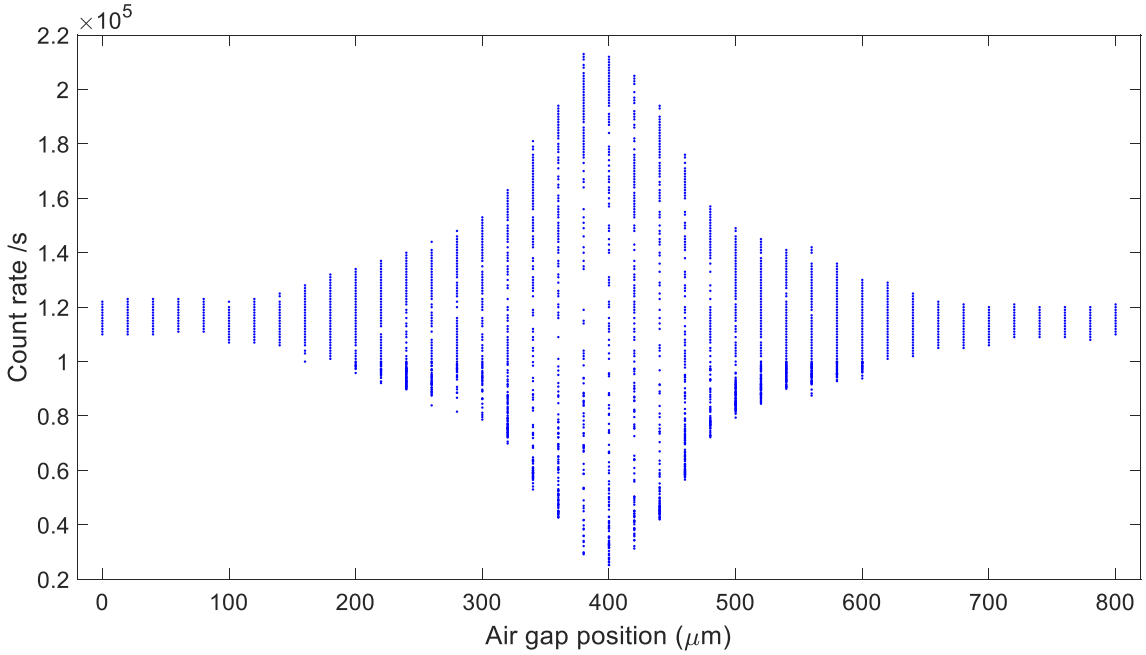

Figure 5-6: Autocorrelation measurement of signal photon coherence time with a 5.6-nm pump. The relative path length is zero at 400 μm air gap position. The single photon coherence time measured is 0.36 ps (FWHM).

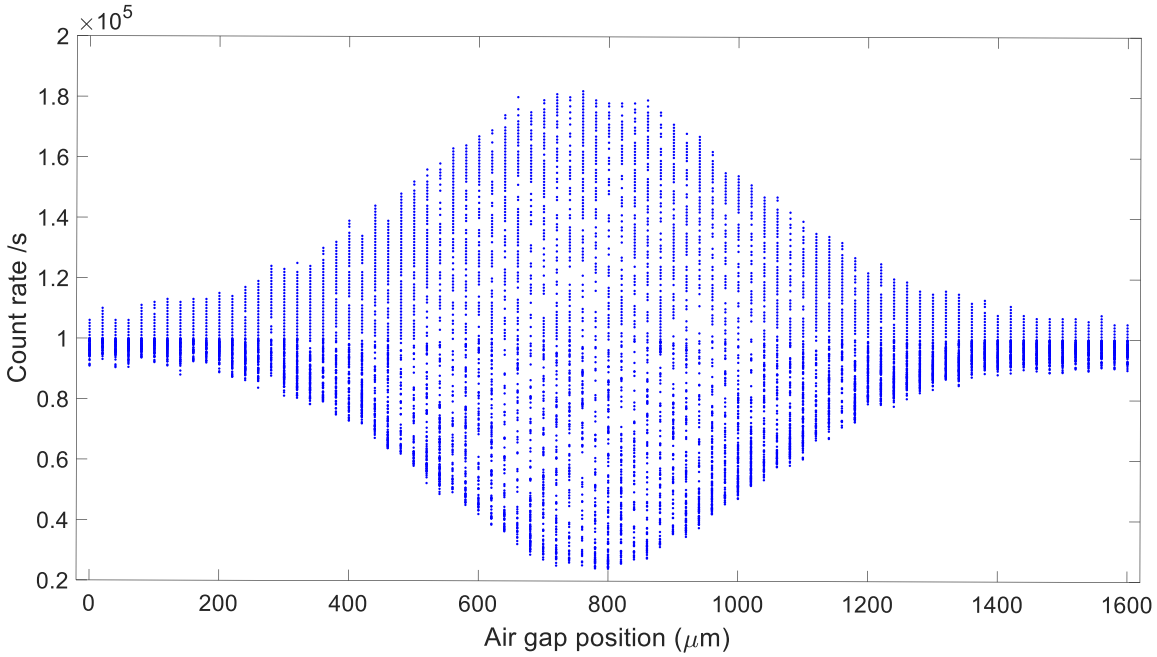

Figure 5-7: Autocorrelation measurement of signal photon coherence time with a 0.95-nm pump. The relative path length is zero at 800 μm air gap position. The single photon coherence time measured is 1.45 ps (FWHM).

Chapter 6

Conclusion and Outlook

6.1 Summary

In this thesis, we have generated and characterized the SPDC biphoton output state under pulsed pumping and extended phase-matching conditions using a custom-fabricated PPKTP crystal that features a Gaussian phase-matching function. Joint spectral density measurements confirm that the Gaussian phase-matching function suppresses to a large extent the side lobes that hinder the generation of a circularly symmetric biphoton state. With the side lobes removed, the SPDC biphotons generated under a pump bandwidth of 0.95 nm can be inferred to have a heralded-state purity of 99% without the use of any spectral filtering in the generation or measurement process, representing the highest purity to date.

Our JSD characterization utilizes two innovative dispersion-based methods to facilitate the measurement procedure. The first is a single-fiber spectrometer that uses a single optical fiber with counter-propagating light, which eliminates the need for two fibers that must be temperature stabilized to maintain equal lengths. The second technique utilizes a commercially available dispersion compensation module with a dispersion amount that can be easily customized and that has low insertion loss of only 2.8 dB. With dispersion equivalent to 100 km of fiber, we were able to obtain the JSD with high resolution and a short acquisition time that should be useful for many spectral analysis tasks in quantum information processing.

Our results demonstrate the unique advantage of SPDC operation under extended

phase-matching conditions that allow orthogonal controls of the joint spectral amplitude of the output biphoton state. We were able to modify the crystal's phase-matching function to have a Gaussian shape, and utilize the pump bandwidth to control the spectral property of the SPDC outputs. At a pump bandwidth of 5.6 nm, we generated strong frequency entanglement between signal and idler that may be useful for photon-efficient quantum communications using high-dimensional frequency encoding [57]. When the pump bandwidth is reduced to 0.95 nm, and assuming the biphoton is transform limited, we obtain signal and idler photons that are ideally suited for generating heralded single photons for many quantum photonic applications that rely on interference between single photons in a single spatiotemporal mode.

In summary, we have completely characterized the spectral properties and the indistinguishablility of the biphotons generated from the custom-fabricated Gaussian phase-matching crystal. We measured a Gaussian-phase matching function as expected and obtained a spectrally factorable state with 99% heralded-state purity at 0.95 nm pump bandwidth. Finally, we showed that the signal and idler are indistinguishable via HOM interferometric measurements.

6.2 Future Research

With the current pump bandwidth control scheme, we used a hard aperture to select the desired frequency components in the frequency domain. The output spectrum resulted from such filtering technique was only approximately Gaussian. To be more specific, when the pump bandwidth was frequency filtered to 0.95 nm, the overlap between the measured pump spectrum and its best fitted Gaussian curve was around 90%, which is shown in Fig. 6-1. For future research, we will investigate how to make the frequency-filtered pump more Gaussian by using a custom-designed apodized filter with semi-transparent regions. The goal of this future research is to have the Gaussian frequency-filtered pump at the 0.95 nm bandwidth, so that 100% heralded-state purity biphoton state can potentially be achieved.

We will also investigate a different experimental setup for JSD measurement where two DCMs are used instead of one. The usage of two DCM eliminates the additional

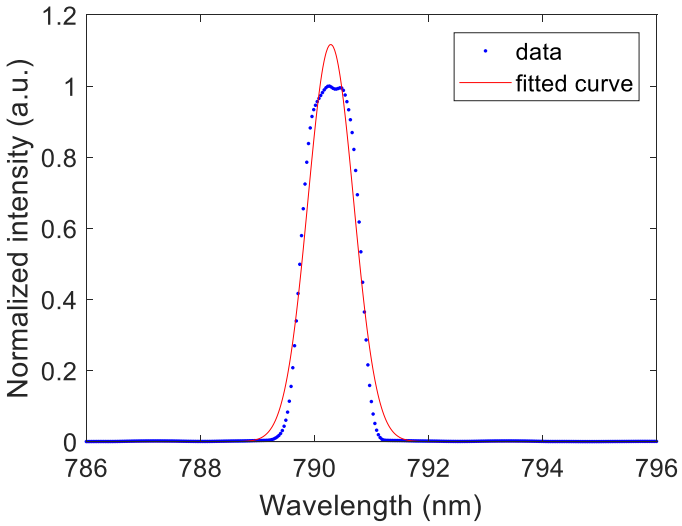

Figure 6-1: Measured spectrum of 0.95-nm pump. The measured data are shown as the blue dots and the best fitted Gaussian is shown as the red curve. $\sim 90\%$ of the area under the fitted curve overlaps the area under the measurement data.

time delay component in the JSD measurement we performed, and reduces the system insertion loss by 3 dB. DCMs with tunable dispersion and a fixed low loss are commercially available and may be worth studying to allow adjustable temporal spread and spectral resolution.

The direct measurement of indistinguishability between individual photons from different SPDC pulses is required to demonstrate the real performance of the heralded single photon source. We will start with interfering heralded single photons from independent SPDC pulses of the same crystal. The first heralded photon will go through a time delay loop while waiting for the second heralded photon. Both photons will then be sent to a 50:50 beam splitter so that their arrival times at the beam splitter are the same. The indistinguishability can then be determined by performing a HOM interference experiment.

Because of fabrication variations, there are differences in performance between different crystals. To exclude any discrepancy caused by the difference in crystals from our experimental results, we restrict our future research plan to using a time multiplexing scheme with only one crystal. However, using two or more crystals for generating independent heralded single photons without time multiplexing should yield a higher photon generation rate. Therefore, the possibility of using more than

one crystal is worth considering. In the future, we would also like to characterize the performance difference between individual crystals as careful characterization of crystal performance variations will be beneficial for scalable implementation of our SPDC heralded single-photon source.

Bibliography

[1] P. Shor, "Algorithms for quantum computation: Discrete logarithms and factoring," Foundations of Computer Science, 1994 Proc., 35th Annual Symposium on. IEEE (1994).

[2] R. Feynman, "Simulating physics with computers," Int. J. Theor. Phys. **21,** 467–488 (1982).

[3] G. Vidal, "Efficient simulation of one-dimensional quantum many-body systems," Phys. Rev. Lett. **93,** 040502 (2004).

[4] L. K. Grover, "A fast quantum mechanical algorithm for database search," Proc. of the 28th annual ACM symposium on Theory of computing, 212–219 (1996).

[5] M. A. Broome, A. Fedrizzi, S. Rahimi-Keshari, J. Dove, S. Aaronson, T. C. Ralph, and A. G. White, "Photonic boson sampling in a tunable circuit," Science **339,** 794–798 (2013).

[6] J. B. Spring, B. J. Metcalf, P. C. Humphreys, W. S. Kolthammer, X.-M. Jin, M. Barbieri, A. Datta, N. Thomas-Peter, N. K. Langford, D. Kundys, J. C. Gates, B. J. Smith, P. G. R. Smith, and I. A. Walmsley, "Boson sampling on a photonic chip," Science **339,** 798–801 (2013).

[7] A. Crespi, R. Osellame, R. Ramponi, D. J. Brod, E. F. Galvao, N. Spagnolo, C. Vitelli, E. Maiorino, P. Mataloni, and F. Sciarrino, "Integrated multimode interferometers with arbitrary designs for photonic boson sampling," Nat. Photon. **7,** 545–549 (2013).

[8] M. Tillmann, B. Dakić, R. Heilmann, S. Nolte, A. Szameit, and P. Walther, "Experimental boson sampling," Nat. Photon. **7,** 540–544 (2013).

[9] A. Politi, J. C. F. Matthews, and J. L. O'Brien, "Shor's quantum factoring algorithm on a photonic chip," Science **325,** 1221 (2009).

[10] J. Mower, N. C. Harris, G. R. Steinbrecher, Y. Lahini, and D. Englund, "High-fidelity quantum state evolution in imperfect photonic integrated circuits," Phys. Rev. A **92,** 032322 (2015).

[11] N. Sangouard, C. Simon, H. de Riedmatten, and N. Gisin, "Quantum repeaters based on atomic ensembles and linear optics," Rev. Mod. Phys. **83,** 33–80 (2011).

[12] K. Azuma, K. Tamaki, and H.-K. Lo, "All-photonic quantum repeaters," Nat. Commun. **6,** 6787 (2015).

[13] C. K. Law, I. A. Walmsley, and J. H. Eberly, "Continuous frequency entanglement: Effective finite Hilbert space and entropy control," Phys. Rev. Lett. **84,** 5304–5307 (2000).

[14] C. K. Law and J. H. Eberly, "Analysis and interpretation of high transverse entanglement in optical parametric down conversion," Phys. Rev. Lett. **92,** 127903 (2004).

[15] P. P. Rohde, W. Mauerer, and C. Silberhorn, "Spectral structure and decompositions of optical states, and their applications," New J. Phys. **9,** 91 (2007).

[16] W. P. Grice, A. B. U'Ren, and I. A. Walmsley, "Eliminating frequency and space-time correlations in multiphoton states," Phys. Rev. A **64,** 063815 (2001).

[17] P. J. Mosley, J. S. Lundeen, B. J. Smith, P. Wasylczyk, A. B. U'Ren, C. Silberhorn, and I. A. Walmsley, "Heralded generation of ultrafast single photons in pure quantum states," Phys. Rev. Lett. **100,** 133601 (2008).

[18] O. Kuzucu, F. N. C. Wong, S. Kurimura, and S. Tovstonog, "Joint temporal density measurements for two-photon state characterization," Phys. Rev. Lett. **101,** 153602 (2008).

[19] T. Gerrits, M. J. Stevens, B. Baek, B. Calkins, A. Lita, S. Glancy, E. Knill, S. W. Nam, R. P. Mirin, R. H. Hadfield, R. S. Bennink, W. P. Grice, S. Dorenbos, T. Zijlstra, T. Klapwijk, and V. Zwiller, "Generation of degenerate, factorizable, pulsed squeezed light at telecom wavelengths," Opt. Express **19,** 24434–24447 (2011).

[20] R.-B. Jin, R. Shimizu, M. Fujiwara, M. Takeoka, R. Wakabayashi, T. Yamashita, S. Miki, H. Terai, T. Gerrits, and M. Sasaki, "Simple method of generating and distributing frequency-entangled qudits," Quantum Sci. Technol. **1,** 015004 (2016).

[21] M. Yabuno, R. Shimizu, Y. Mitsumori, H. Kosaka, and K. Edamatsu, "Four-photon quantum interferometry at a telecom wavelength," Phys. Rev. A **86,** 010302(R) (2012).

[22] R.-B. Jin, R. Shimizu, K. Wakui, H. Benichi, and M. Sasaki, "Widely tunable single photon source with high purity at telecom wavelength," Opt. Express **21,** 10659–10666 (2013).

[23] G. Harder, V. Ansari, B. Brecht, T. Dirmeier, C. Marquardt, and C. Silberhorn, "An optimized photon pair source for quantum circuits," Opt. Express **21,** 13975–13985 (2013).

[24] T. Gerrits, F. Marsili, V. B. Verma, L. K. Shalm, M. Shaw, R. P. Mirin, and S. W. Nam, "Spectral correlation measurements at the Hong-Ou-Mandel interference dip," Phys. Rev. A **91,** 013830 (2015).

[25] F. Kaneda, K. Garay-Palmett, A. B. U'Ren, and P. G. Kwiat, "Heralded single-photon source utilizing highly nondegenerate, spectrally factorable spontaneous parametric downconversion," Opt. Express **24,** 10733–10747 (2016).

[26] M. M. Weston, H. M. Chrzanowski, S. Wollmann, A. Boston, J. Ho, L. K. Shalm, V. B. Verma, M. S. Allman, S. W. Nam, R. B. Patel, S. Slussarenko, and G. J. Pryde, "Efficient and pure femtosecond-pulse-length source of polarization-entangled photons," Opt. Express **24,** 10869–10879 (2016).

[27] V. Giovannetti, L. Maccone, J. H. Shapiro, and F. N. C. Wong, "Generating entangled two-photon states with coincident frequencies," Phys. Rev. Lett. **88,** 183602 (2002).

[28] V. Giovannetti, L. Maccone, J. H. Shapiro, and F. N. C. Wong, "Extended phase-matching conditions for improved entanglement generation," Phys. Rev. A **66,** 043813 (2002).

[29] P. B. Dixon, J. H. Shapiro, and F. N. C. Wong, "Spectral engineering by Gaussian phase-matching for quantum photonics," Opt. Express **21,** 5879–5890 (2013).

[30] M. Y. Niu, F. N. C. Wong, and J. H. Shapiro, in preparation.

[31] C. Chen, B. Cao, M. Y. Niu, F. Xu, Z. Zhang, J. H. Shapiro, F. N. C. Wong, and C. W. Wong, "Harnessing high-dimensional hyperentanglement through a biphoton frequency comb," Opt. Express **25,** 7300–7312 (2017).

[32] R. Erdmann, D. Branning, W. Grice, and I. A. Walmsley, "Restoring dispersion cancellation for entangled photons produced by ultrashort pulses," Phys. Rev. A **62,** 5879–5890 (2000).

[33] W. Grice, R. Erdmann, I. A. Walmsley, and D. Branning, "Spectral distinguishability in ultrafast parametric down-conversion," Phys. Rev. A **57,** R2289 (1998).

[34] T. E. Keller, and M. H. Rubin, "Theory of two-photon entanglement for spontaneous parametric down-conversion driven by a narrow pump pulse," Phys. Rev. A **56,** 1534–1541 (1997).

[35] R.B. Jin, R. Shimizu, K. Wakui, M. Fujiwara, T. Yamashita, S. Miki, H. Terai, Z. Wang, and M. Sasaki, "Pulsed Sagnac polarization-entangled photon source with a PPKTP crystal at telecom wavelength," Opt. Express **22,** 11498–11507 (2014).

[36] A. B. U'Ren, C. Silberhorn, R. Erdmann, K. Banaszek, W. P. Grice, I. A. Walmsley, and M. G. Raymer, "Generation of pure-state single-photon wavepackets by conditional preparation based on spontaneous parametric downconversion," Laser Phys. **15,** 146–161 (2005).

[37] P. J. Mosley, J. S. Lundeen, B. J. Smith, and I. A. Walmsley, "Conditional preparation of single photons using parametric downconversion: a recipe for purity," New J. Phys. **10,** 093011 (2008).

[38] R. Erdmann, D. Branning, W. Grice, and I. A. Walmsey, "Restoring dispersion cancellation for entangled photons produced by ultrashort pulses," Phys. Rev. A **62,** 053810 (2000).

[39] O. Kuzucu, M. Fiorentino, M. A. Albota, F. N.C. Wong, and F. X. Kärtner, "Two-photon coincident-frequency entanglement via extended phase matching," Phys. Rev. Lett. **94,** 083601 (2005).

[40] A. Eckstein, A. Christ, P. J. Mosley, and C. Silberhorn, "Highly efficient single-pass source of pulsed single-mode twin beams of light," Phys. Rev. Lett. **106,** 013603 (2011).

[41] F. Knig, F. N. C. Wong, "Extended phase matching of second-harmonic generation in periodically poled $KTiOPO_4$ with zero group-velocity mismatch," Appl. Phys. Lett. **84,** 1644-1646 (2004).

[42] L. Zhang, C. Slller, O. Cohen, B. J. Smith, I. A. Walmsley, "Heralded generation of single photons in pure quantum states," J. Mod. Opt. **59,** 1525-1537 (2012).

[43] A. M. Brańczyk, A. Fedrizzi, T. M. Stace, T. C. Ralph, and A. G. White, "Engineered optical nonlinearity for quantum light sources," Opt. Express **19,** 55–65 (2011).

[44] M. M. Fejer, G. A. Magel, D. H. Jundt, and R. L. Byer, "Quasi-phase-matched second harmonic generation: tuning and tolerances," Quantum Electron. **28,** 2631–2654 (1992).

[45] M. Avenhaus, A. Eckstein, P. J. Mosley, and C. Silberhorn, "Fiber-assisted single-photon spectrograph," Opt. Lett. **34,** 2873–2875 (2009).

[46] A. M. Weiner, J. P. Heritage, and E. M. Kirschner, "High-resolution femtosecond pulse shaping," J. Opt. Soc. Am. B **5,** 1563–1572 (1988).

[47] A. M. Weiner, "Femtosecond pulse shaping using spatial light modulators," Rev. Sci. Instrum. **71,** 1929–1960 (2000).

[48] R. S. Bennink, "Optimal collinear Gaussian beams for spontaneous parametric down-conversion," Phys. Rev. A **81,** 053805 (2010).

[49] P. B. Dixon, D. Rosenberg, V. Stelmakh, M. E. Grein, R. S. Bennink, E. A. Dauler, A. J. Kerman, R. J. Molnar, and F. N. C. Wong, "Heralding efficiency and correlated-mode coupling of near-IR fiber-coupled photon pairs," Phys. Rev. A **90,** 043804 (2014).

[50] R.-B. Jin, K. Wakui, R. Shimizu, H. Benichi, S. Miki, T. Yamashita, H. Terai, Z. Wang, M. Fujiwara, and M. Sasaki, "Nonclassical interference between independent intrinsically pure single photons at telecommunication wavelength," Phys. Rev. A **87,** 063801 (2013).

[51] N. Bruno, A. Martin, T. Guerreiro, B. Sanguinetti, and R. T. Thew, "Pulsed source of spectrally uncorrelated and indistinguishable photons at telecom wavelengths," Opt. Express **22,** 17246–17253 (2014).

[52] P. S. Kuo, T. Gerrits, V. Verma, S. W. Nam, O. Slattery, L. Ma, and X. Tang, "Characterization of type-II spontaneous parametric down-conversion in domain-engineered PPLN," Proc. SPIE **9762,** 976211 (2016).

[53] R.-B. Jin, T. Gerrits, M. Fujiwara, R. Wakabayashi, T. Yamashita, S. Miki, H. Terai, R. Shimizu, M. Takeoka, and M. Sasaki, "Spectrally resolved Hong-Ou-Mandel interference between independent photon sources," Opt. Express **23,** 28836–28848 (2015).

[54] C. K. Hong, Z. Ou, and L. Mandel, "Measurement of subpicosecond time intervals between two photons by interference," Phys. Rev. Lett. **59,** 2044 (1987).

[55] M. B. Nasr, B. EA Saleh, A. V. Sergienko, and M. C. Teich, "Demonstration of dispersion-canceled quantum-optical coherence tomography," Phys. Rev. Lett. **91,** 083601 (2003).

[56] S. Lloyd, J. H. Shapiro, and F. N. C. Wong, "Quantum magic bullets by means of entanglement," J. Opt. Soc. Am. B **19,** 312 (2002).

[57] Z. Xie, T. Zhong, S. Shrestha, X. Xu, J. Liang, Y.-X. Gong, J. Bienfang, A. Restelli, J. H. Shapiro, F. N. C. Wong, and C. W. Wong, "Harnessing high-dimensional hyperentanglement through a biphoton frequency comb," Nat. Photon. **9,** 536–542 (2015).